

博士論文

Theoretical studies on the reaction path of hydrogen transfer  
with many-body effects

(水素移動反応の多体効果を考慮した反応経路に関する理論的研究)

黒木 彩香



## Abstract

Proton transfer reaction with strong couplings of skeletal vibration with reaction coordinate often occurs and *ab initio* molecular dynamics simulations are useful for the analyzing mechanisms involved in many-body effects and bond rearrangement.

MD trajectories have coordinates information, however the geometry information is characteristic to each system. In order to translate the coordinates into general electronic structures, I applied the valence bond (VB) theory. This theory assumes that all bonds are localized bonds formed between two atoms by the donation of an electron from each atom, and may be related to geometry information.

I performed *ab initio* MD calculation in protonated benzene as model system related in many-body effects as strong couplings of skeletal vibration with reaction coordinate, and explained the change of electronic states by VB theory. It is found that the  $sp^2$  hybridizations on adjacent two carbon atoms repel the transferred proton. Moreover I analyzed the reaction cycle of dehydrogenation reaction in ammonia borane catalyzed by iron complex. In the same way of protonated benzene,  $sp^2$  hybridizations tend to release hydrogens and the activation barrier is lowered by providing the enough space to make planar  $NH_2BH_2$  with a rotation of bulky ligand.

Examine of proton transfer reactions considering the many-body effects lead to make clear the behavior of the number of degrees of freedom around them.



# Contents

Abstract	iii
Chapter 1. General introduction	<b>1</b>
Chapter 2. Methodology	<b>6</b>
2.1 <i>Ab initio</i> molecular dynamics	6
2.2 Theories of chemical bonding	7
2.3 Bader's Atoms in Molecules Theory	8
2.4 Population analyses	10
Chapter 3. Proton transfer in protonated benzene	<b>14</b>
3.1 Electronic characteristics of protonated benzene	14
3.2 Calculation methods	16
3.3 Lifetime distribution	19
3.4 Definition of relative coordinate of proton in trajectories	22
3.5 Electronic states of the carbon atoms	26
3.6 Electronic states for non-statistical lifetime distribution	29
3.7 Conclusions	32
Chapter 4. Ammonia borane dehydrogenation	<b>34</b>
4.1 Ammonia borane dehydrogenation reaction for H <sub>2</sub> storage	34
4.2 Calculation methods	39
4.3 Electronic states and influence of the phenyl group	42
4.4 Energy profiles of the reaction cycle	49
4.5 Reactivity difference among the PMe <sub>3</sub> and PMe <sub>2</sub> Ph groups	53
4.6 Electron-donation by the OMe group	59
4.7 Conclusions	60
Chapter 5. Discussion	<b>62</b>

Chapter 6. General conclusions	<b>66</b>
Acknowledgements	69
Appendix	72
Bibliography	76

# Chapter 1

## General Introduction

Chemical reactions occur on a wide range of timescales. Elementary steps in chemistry, such as the dynamical event of a single-bond rearrangement, appear to take place on femtosecond to picosecond timescales [1]. One of the advantages of computational chemistry is to be able to calculate the energy and structure in each step of reactions.

Examples of ultrafast chemistry include proton transfer, electron transfer, bond fissions and cis-trans isomerizations. Proton occupies a special position as a promoter and mediator in various chemical reactions, especially organic chemistry occurring in solution [2]. In recent years, the important substrate water molecules in photosynthesis are identified among the many water molecules around  $\text{Mn}_4\text{CaO}_5$  cluster in Photosystem II [3]. It revealed what is the route of release of protons generating with oxygen in water-splitting reaction. The proton transfer reaction path would make it possible to identify the active site of the water-splitting reaction in  $\text{Mn}_4\text{CaO}_5$  cluster. Proton is just a “mediator” in the system, however, it plays a very important part for understanding the main points of the whole reaction mechanism. “Mediators” often play

a role in reflectors toward the surrounding environments. Their behaviors are always affected by the environments, therefore we can understand about the environments by following them. In the same way, to understand the reaction path of proton transfer often leads to find the reasonable reaction path in the whole system, since the mechanism of proton transfer reactions reflect electronic state around it. Therefore proton transfer is very important as elementary processes of various chemical reactions.

However there are some features that make it difficult to investigate the reaction mechanisms for proton transfer. Solvent controls the reaction coordinate and makes the path complicated because of hydrogen bonding [4]. Quantum tunneling of hydrogen occurs [5]. Moreover strong couplings of skeletal vibration with reaction coordinate are involved in the reaction path [6].

In the last decades, *ab initio* molecular dynamics simulations have significantly contributed to the improvement of our understanding of mechanism of proton transfer reactions. At the heart of the techniques lies the crucial idea of computing the many-body interactions by solving the electronic structure problem "on the fly" as the simulation proceeds [7]. From the obtained data of trajectories, geometry information is often used to explain the mechanism of the reactions. In the case of proton transfer reactions of dioxonium ion ( $\text{H}_3\text{O}_2^+$ ), the barrier height of the proton transfer is very high at larger values of the distances between the two oxygen atoms,  $R_{\text{O-O}}$  ( $> 2.5$  Å), whereas it reduces remarkably with smaller values of  $R_{\text{O-O}}$  ( $\sim 2.4$  Å) and vanishes at very

small  $R_{O-O}$  ( $< 2.3 \text{ \AA}$ ) [8]. The distance between proton and the donor or acceptor atom has been used in describing Brønsted acid strength since proton transfer is acid-base reaction. However, the geometry information is peculiar to each system. Actually, the mechanisms of proton transfer can be practical use to explain the surroundings because they involve the information of the number of degrees of freedom.

Accordingly, I bring the information of electronic states into the trajectories of proton transfer reactions with many-body effects obtained by *ab initio* MD calculations. The theory for describing the electronic states is equivalent to the theories of chemical bonding. The theories of chemical bonding are mainly represented by valence bond (VB) theory and molecular orbital (MO) theory. MO theory provides detailed bonding picture by analyzing the energy and orbitals, but it does not give any idea of molecular geometry. The order of the molecular orbitals does not conserved with the MD trajectories. What is indicated is the theory corresponded to geometry information. For example, Bader's Atoms in Molecules theory is the tool for bonding analyses based on electron density. Thus this theory indirectly involves geometry information. It is available for relatively simple molecules, such as planar structure. On the other hand, VB theory assumes that all bonds are localized bonds formed between two atoms by the donation of an electron from each atom. It is essentially equal to Lewis model. Owing to this, the concept originally explains the structure of stable states, but can be corresponded to any other structures.

VB theory is also popular to help to find some regulations and predict reaction mechanisms because of its simple system. Therefore, VB theory may be useful to convert MD trajectories into electronic information.

In this study, I performed *ab initio* MD calculation in model system related in many-body effects as strong couplings of skeletal vibration with reaction coordinate, and explained the change of electronic states by VB theory (Chapter 3). Moreover I analyzed the fundamental process of dehydrogenation reaction and referred about the main points of catalytic activity while using the analyses (Chapter 4).



## Chapter 2

### Methodology

#### 2.1 *Ab initio* molecular dynamics

Steps in molecular simulations are as follows:

1. Give initial coordinates and velocities
2. Compute forces on each atom from energy expression
3. Integrate Newton's equations of motions, and update the coordinates and velocities
4. Repeat above 1 to 3, and compute structural, dynamical, thermodynamic and statistical properties from the obtained trajectories

At the step 2, *ab initio* MD methods solve the electronic Schrödinger equation in order to determine the forces acting on the atoms. Therefore *ab initio* MD simulations allow arbitrary bond rearrangement. It means that this method does not use fixed model potential but is performed “on the fly”, while it can investigate many-body interactions as classical molecular dynamics simulation.

MD trajectory has both coordinates and velocity information. Therefore it is useful for understanding the electronic states to analyze by the theory relevant to geometry.

## 2.2 Theories of chemical bonding

### 2.2.1 Valence bond theory

Valence bond (VB) theory has its roots in Gilbert Newton Lewis's paper, "The Atom and The Molecule" [9] in 1916. Lewis model and the valence shell electron pair repulsion rule (VSEPR), that assumes that each atom in a molecule will achieve a geometry that minimizes the repulsion between electrons in the valence shell of that atom, had been constructed in order to describe the molecular structures without quantum mechanics (QM). After the development of QM in 1925-26 by Heisenberg, Schrödinger, Born and Dirac, Heitler and London came up with the idea that resonance and wave functions contributed to chemical bonds, in which they used dihydrogen as an example [10]. This theory assumes that all bonds are localized bonds formed between two atoms by the donation of an electron from each atom.

In fact, their theory was equivalent to Lewis's theory, with the difference of quantum mechanics being used. Nonetheless, Heitler and London's theory proved to be successful providing Pauling and Slater with the idea of resonance effects and hybridization to represent delocalize electronic states. Valence bond theory also involves covalent-ionic superposition and atomic orbital overlap to describe chemical bonds.

### 2.2.2 Molecular orbital theory

Molecular orbital (MO) theory assumes electrons are not assigned to individual bonds between atoms, but are treated as moving under the influence of the nuclei in the whole molecule. It utilizes symmetry and group theory, and describes relatively local interaction of orbitals.

MO theory provides detailed bonding picture by analyzing the energy and orbitals, while it does not give any idea of molecular geometry.

### 2.3 Bader's Atoms in Molecules Theory

This is the bonding analysis based on electron density. The Bader's atoms in molecules theory is a tool for prediction of the properties and reactivity of molecular structures [11]. The distribution function of the electron density  $\rho(r)$  is a key concept in the AIM theory. The  $\rho(r)$  function can be obtained from both the results of quantum chemical calculations and the precision X-ray diffraction studies.

The Hessian matrix of the electron density is as follows:

$$H(\mathbf{r}) = \begin{pmatrix} \frac{\partial^2 \rho(\mathbf{r})}{\partial x^2} & \frac{\partial^2 \rho(\mathbf{r})}{\partial x \partial y} & \frac{\partial^2 \rho(\mathbf{r})}{\partial x \partial z} \\ \frac{\partial^2 \rho(\mathbf{r})}{\partial y \partial x} & \frac{\partial^2 \rho(\mathbf{r})}{\partial y^2} & \frac{\partial^2 \rho(\mathbf{r})}{\partial y \partial z} \\ \frac{\partial^2 \rho(\mathbf{r})}{\partial z \partial x} & \frac{\partial^2 \rho(\mathbf{r})}{\partial z \partial y} & \frac{\partial^2 \rho(\mathbf{r})}{\partial z^2} \end{pmatrix}. \quad (2.1)$$

The Laplacian of the electron density is the trace of the Hessian matrix. That is:

$$D(\mathbf{r}_{\text{CP}}) = \begin{pmatrix} \frac{\partial^2 \rho(\mathbf{r})}{\partial x'^2} & 0 & 0 \\ 0 & \frac{\partial^2 \rho(\mathbf{r})}{\partial y'^2} & 0 \\ 0 & 0 & \frac{\partial^2 \rho(\mathbf{r})}{\partial z'^2} \end{pmatrix} = \begin{pmatrix} \lambda_1 & 0 & 0 \\ 0 & \lambda_2 & 0 \\ 0 & 0 & \lambda_3 \end{pmatrix}. \quad (2.2)$$

Bader has shown that the function  $\rho(\mathbf{r})$  for a given polyatomic system, as well as many critical points (CP) of electron density (the  $\rho(\mathbf{r})$  gradient in the critical point is zero) determine completely and uniquely the molecular structure of a system. A critical point in  $\rho(\mathbf{r})$  is classified by the rank  $\omega$  (the number of nonzero eigenvalues  $\lambda_i$ ) and the signature  $\sigma$  (the algebraic sum of the signs of the eigenvalues  $\lambda_i$ ) of the Hessian matrix. For a rank = 3, there are only four possible types of critical points:

(1) critical point (3, -3) means local maximum ( $\lambda_1, \lambda_2, \lambda_3 < 0$ ) and corresponds to the nuclear position in the space;

(2) critical point (3, -1) means maximum in two directions and minimum in one direction ( $\lambda_1, \lambda_2 < 0, \lambda_3 > 0$ ), that is an indicator for the bonding interactions and the type is named in bond critical point (BCP);

(3) critical point (3, +1) means maximum in one direction and minimum in two directions ( $\lambda_1 < 0, \lambda_2, \lambda_3 > 0$ ), which corresponds to the formation of a ring and the type is ring critical point (RCP);

(4) critical point (3, +3) means local minimum ( $\lambda_1, \lambda_2, \lambda_3 > 0$ ) which corresponds to the formation of polyhedral (cellular) structure and the type is cage critical point (CCP).

The reliability of the number of critical points found in a structure can be checked by the Poincaré - Hopf equation:

$$n_{AP} - n_{BCP} + n_{RCP} - n_{CCP} = 1. \quad (2.3)$$

In this way, topology of the electron density provides the concepts of atoms, bonds and structure.

These concepts are applicable not limited to stable structures like Lewis model and VSEPR model, but to transition states and any other structures.

## 2.4 Population analyses

### 2.4.1 Mulliken population analysis

Mulliken charges arise from the Mulliken population analysis advocated in 1955 [12]. It is based on the linear combination of atomic orbitals and therefore the wave function of the molecule. The electrons are partitioned to the atoms based on the nature of the atomic orbitals'

contribution to the molecular wave function. Generally, the total number of electrons in the molecule  $N$  can be expressed as:

$$\begin{aligned}
 N &= \sum_j^{electrons} \int \psi_j(r_j) \psi_j(r_j) dr_j \\
 &= \sum_j^{electrons} \sum_{r,s} \int c_{jr} \phi_r(r_j) c_{js} \phi_s(r_j) dr_j \\
 &= \sum_j^{electrons} \left( \sum_r c_{jr}^2 + \sum_{r \neq s} c_{jr} c_{js} S_{rs} \right) \quad (2.4)
 \end{aligned}$$

where  $r$  and  $s$  index the AO basis functions  $\phi$ ,  $c_{jr}$  are coefficients of the basis function  $r$  in the MO  $j$ , and  $S$  is the overlap matrix defined before. This shows that the total number of electrons can be divided into two sums: the first one including only squares of single AO basis function ( $r$ ), and the other one products of two different AO functions ( $r$  and  $s$ ). The first term can be thought of as electrons belonging to the particular atom. The second term makes it complicated how to divide the shared electrons between the two atoms.

Mulliken suggested to split the shared density 50:50. Then the electrons associated with the atom  $k$  are given by:

$$\begin{aligned}
 N_k &= \sum_j^{electrons} \left( \sum_{r \in k} c_{jr}^2 + \sum_{r,s \in k, r \neq s} c_{jr} c_{js} S_{rs} \right. \\
 &\quad \left. + \sum_{r \in k, s \notin k} c_{jr} c_{js} S_{rs} \right). \quad (2.5)
 \end{aligned}$$

It works well for comparing changes in partial charge assignment between two different geometries when the same size basis set is used.

$$q_k = Z_k - N_k \quad (2.6)$$

## 2.4.2 Natural charge

Natural charge is based on natural bond orbital scheme [13]. It was evolved from around 1980.

While Mulliken population analysis localizes orbitals based on basis functions, natural bond analysis localizes orbitals into three distinct groups: non-bonding natural atomic orbitals (NAOs), orbitals involved in bonding and antibonding (NBOs), and Rydberg type orbitals. NAO is acquired by block diagonalization of density matrix for angular momenta in each atomic orbital. The NAOs and Rydberg type orbitals are made up of basis sets of single atoms and the NBOs are a combination of basis set atomic orbitals of two atoms. Based on this model of electron partitioning, natural population analysis treats the NBOs as the Mulliken method treats all the orbitals. This scheme makes it possible to estimate donor-acceptor (bond-antibond) interactions [14].

This method differentiates between the orbitals that will overlap to form a bond and those that are too near the core of an atom to be involved in bonding. This leads convergence of atomic partial charge to a stable value as the basis set size is increased.



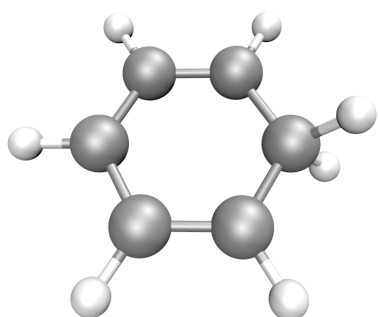
## Chapter 3

### Proton transfer in protonated benzene

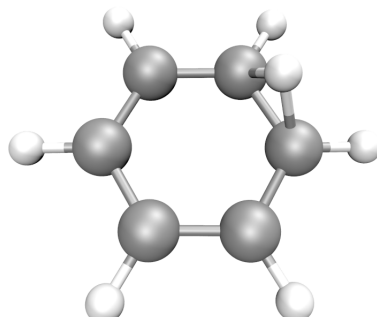
#### 3.1 Electronic characteristics of protonated benzene

As is shown in an example of strong coupling of skeletal vibration with reaction coordinate, I focused on protonated benzene ( $C_6H_7^+$ ) and investigated on the mechanism of intramolecular proton transfer. The protonated benzene has been previously studied as an intermediate species in various electrophilic aromatic substitution reactions. According to such previous studies[15][16], the  $\sigma$ -complex represents the global minimum along the calculated  $C_6H_7^+$  potential (Figure 3.1(a)). The bridged structure (Figure 3.1(b)) is predicted to be the lowest transition state for proton migration between equivalent sigma complexes, with an activation barrier of  $E_a = 6.2 \sim 10.4 \text{ kcal mol}^{-1}$ . When an additional proton is attached to a given carbon atom on the benzene ring, that carbon having two protons will generate  $sp^3$  hybrid orbitals, while the other carbons, each having only one proton, will have  $sp^2$  hybrid orbitals. Therefore, the proton transfer reaction should occur in conjunction with a change in the hybridization of carbon atoms.

(a)



(b)



---

FIGURE 3.1: Stable structure (a) and transition state structure in intramolecular proton transfer (b) of protonated benzene

## 3.2 Calculation methods

I initially examined the energetics to see the outline of proton transfer in protonated benzene by quantum chemistry calculations. The first step was a survey of the activation energies on the potential surface using the second order Moller-Plesset perturbation theory (MP2) [17]–[22] and the density functional theory [23][24][25] with B3LYP functional (B3LYP) [26][27] with 3-21G, 6-31G(d) and 6-31G(d, p) basis sets. The calculated activation energies are summarized in Table 1. The activation energy obtained using the MP2/ 6-31G(d, p) was 7.86 kcal/mol, which is consistent with range of values from 6.2 to 10.4 kcal/mol determined experimentally [16][28]. For this reason, the MP2 method together with the 6-31G(d, p) basis set was used through the remainder of the study.

In order to examine the coupling between proton transfer and the hybridization of carbon atoms, all degrees of freedom must be treated equally. As such, I performed the *ab initio* molecular dynamics calculations [29] to examine the mechanism of proton transfer reaction in protonated benzene. The potential derivatives were obtained by employing the GAMESS software package[30]. And the Gear predictor-corrector method [31] was used to integrate the nuclear equations of motion, applying an integration time step of 0.2 fs.

The initial conditions for sampled trajectories were chosen as follows. As shown in Figure 3.1(a), there are two  $sp^3$  protons in protonated benzene, one of which was labeled H(7). I

initially sampled the position of H(7),  $r_{\text{initial,H(7)}}$ , at random around the optimized position of each atom,  $r_{\text{opt,H(7)}}$ , maintaining the value of  $|r_{\text{initial,H(7)}} - r_{\text{opt,H(7)}}|$  below 0.5 Å. In addition, the position of the other atom,  $r_{\text{initial}}$  was randomly sampled around the optimized position of each atom,  $r_{\text{opt}}$  keeping  $|r_{\text{initial}} - r_{\text{opt}}|$  below 0.2 Å. In this manner, a total of 284 initial structures were selected, after which each trajectory was integrated, applying zero initial momenta. After running the trajectories for 10 fs, I reset the total energy while maintaining zero total angular momentum. The momenta were scaled to attain a total energy of  $E = 3.765$  eV for the optimized structure, a value that is 0.5 eV higher than the zero point vibrational energy of the system. I used these positions and momenta as the initial conditions for the trajectories. Each trajectory calculated was run over 500 fs and the ensemble of sampled trajectories contained a total 700 proton transfers.

TABLE 3.1: Effects of calculation method on activation energy (kcal mol<sup>-1</sup>)

	3-21G	6-31G(d)	6-31G(d,p)
B3LYP	18.34	13.97	12.99
MP2	16.42	9.372	7.863

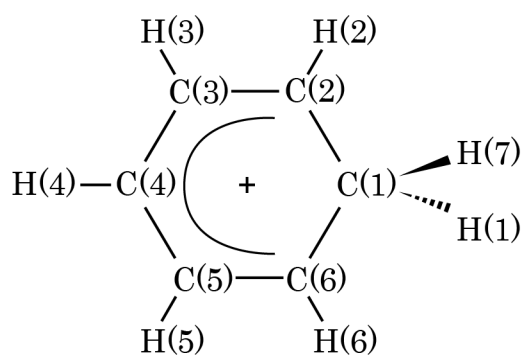


FIGURE 3.2: Labels of the atoms

### 3.3 Lifetime distribution

The time-scale of proton transfers was initially examined. The relative coordinates specifying the position of a proton, H, in between the two carbon atoms, C(1) and C(2), may be defined as

$$\gamma = R_{C(1)-H} \cos \theta_{HCC} / R_{C(1)-C(2)} \quad (3.1)$$

where  $R_{C(1)-C(2)}$  and  $R_{C(1)-H}$  are the distances between C(1) and C(2), and C(1) and H, respectively, and  $\theta_{HCC}$  is the H-C(1)-C(2) angle. A value of the relative coordinate,  $\gamma$ , of less than 0.5 indicates that the proton is located nearer the C(1) than the C(2) atom. As such, I defined the proton transfer transition time during each trajectory as occurring at the moment at which  $\gamma = 0.5$ . The time lag between the proton transfer reactions, equal to the lifetime of each stable protonated benzene structure, was first examined. Figure 3.3 presents the lifetime distribution obtained from *ab initio* molecular dynamics calculations. Based on a statistical assumption, the distribution of the lifetime may be derived as follows [32]

$$P(t) = A \exp[-k(E)t] \quad (3.2)$$

where  $P(t)$  is the probability of a given lifetime,  $t$ ,  $A$  is a constant, and  $k(E)$  is the rate constant that varies with the total energy,  $E$ . Based on the RRK theory, the reaction rate may be estimated as

$$k(E) = \nu \left( \frac{E - E_0}{E} \right)^{s-1} \quad (3.3)$$

where  $\nu$  is the frequency along the reaction coordinate,  $E_0$  is the activation energy and  $s$  is the

degrees of freedom [33][34]. According to Equation (3.2), a log plot of  $P(t)$  should generate a linear relationship, as indicated by the red line in Figure 3.3. It is evident that, at times longer than 75 fs, the plot of  $P(t)$  is indeed almost linear. However, the dynamically calculated lifetime distribution contains a large number of short lifetime trajectories at  $t < 50$  fs, which is not in agreement with the hypothetical statistical outcome.

One possible reason for the large number of short lifetime trajectories is the phenomenon of “direct trajectories” [35]. A direct trajectory is one that crosses the transition state just after the onset of sampling. These trajectories do not interact strongly with the other modes of the system and it is known that they may lead to non-RRKM characteristics in the lifetime distribution. To remove the effects of the direct trajectories from the lifetime distribution, I started sampling just after initial occurrence of  $\gamma = 0.5$ , as shown by dotted line in Figure 3.3. However, even when the effects of direct trajectories are excluded, the lifetime distribution still contains a significant quantity of values at short times, demonstrating that the large number of short lifetime proton transfers cannot be explained by the presence of direct trajectories.

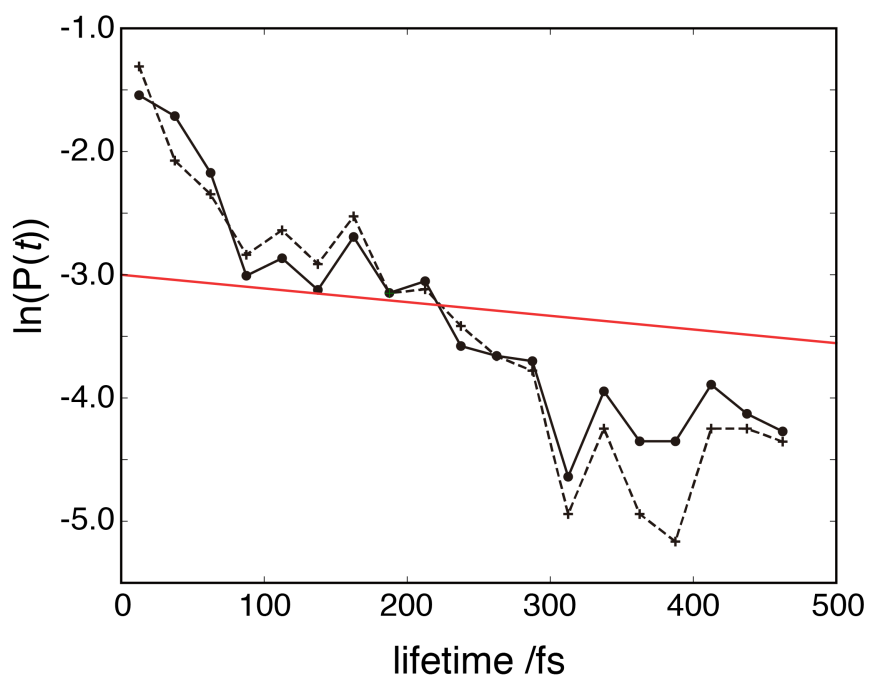


FIGURE 3.3: Lifetime distribution. Red line shows approximate slope based on RRK theory.

### 3.4 Definition of relative coordinate of proton in trajectories

To determine the cause of the large quantity of short lifetime trajectories, I subsequently analyzed a typical example trajectory. Here, I first define new relative coordinates,  $\alpha(i)$  and  $\beta(i)$ , for each hydrogen atom  $H(i)$ , to examine the motion of hydrogen atoms along the trajectories as follows (Figure 3.2).

I initially assume that the hydrogen atom,  $H(i)$ , is located between two carbon atoms:  $C(j)$  and  $C(j+1)$ . The center of gravity of the six membered ring is set to  $G$ , and the vector  $GH'(i)$  is defined as a projection of the  $GH(i)$  vector on a plane containing three points:  $G$ ,  $C(j)$ , and  $C(j+1)$ . The  $GH'(i)$  vector is thus located just between  $GC(j)$  and  $GC(j+1)$  vectors. The relative coordinate,  $\alpha(i)$ , is defined as

$$\alpha(i) = \frac{\angle C(j)GH'(i)}{\angle C(j)GC(j+1)} \quad (3.4)$$

where  $\angle C(j)GC(j+1)$  and  $\angle C(j)GH'(i)$  are the angles between lines  $C(j)G$  and  $GC(j+1)$ , and  $C(j)G$  and  $GH'(i)$ , respectively. The relative coordinate,  $\alpha(i)$ , is almost 0 when  $H(i)$  is located near  $C(j)$ , while  $\alpha(i)$  is almost 1 when  $H(i)$  is located near  $C(j+1)$ . A value of 0.5 for this term indicates that the hydrogen atom  $H(i)$  is at the center point between  $C(j)$  and  $C(j+1)$ . I may also define the angle,  $\beta(i)$ , corresponding to the position of hydrogen atom  $H(i)$  perpendicular to the benzene ring as

$$\beta(i) = \angle H(i)GH'(i). \quad (3.5)$$

When  $H(i)$  is presented in the plane containing the three point  $G$ ,  $C(j)$ , and  $C(j+1)$ ,  $\beta(i)$  is  $0^\circ$ .

The values of  $\beta(1)$  and  $\beta(7)$  in the stable structure of protonated benzene given in Figure 3.1(a) are  $-21.7$  and  $21.7^\circ$ , severally.

The  $\alpha(i)$  values for each hydrogen atom,  $H(i)$ , along a sample trajectory are summarized in Figure 3.4(a) as functions of time. In order to show all  $\alpha(i)$  in the same graph, I plotted  $\alpha(i) + (j - 1)$  for six carbon atoms,  $C(1) - C(6)$ . In the initial structure, the  $H(7)$  and  $H(1)$  atoms are both located on the same carbon atom,  $C(1)$ . The solid thick line shows the value of  $\alpha(7)$  corresponding to the position of hydrogen  $H(7)$ , while the dotted line represents the motion of  $H(1)$ . The solid line demonstrates that  $H(7)$ , transfers from  $C(1)$  in the direction of  $C(2)$  at  $t = 37.0$  fs, although it is subsequently trapped between  $C(1)$  and  $C(2)$  until  $t = 60.2$  fs. During this period,  $H(7)$  frequently transfers or vibrates between  $C(1)$  and  $C(2)$ .  $H(7)$  passes through an equidistant position at  $\alpha(7) = 0.5$  several times and the proton transfer takes place a total of four times throughout this period. Following this,  $H(7)$  once again returns to  $C(1)$  and then moves back to  $C(2)$  again, and is once more trapped between the two carbons over the time span of 115 to 150 fs. In this period, the proton transfer once again occurs four times and eventually  $H(7)$  moves to  $C(2)$  for a fifth time at 169.0 fs, at which point  $H(2)$  and  $H(7)$  are attached to the same carbon atom,  $C(2)$ . The  $H(2)$  atom, as indicated by the dashed-dotted line, is located in the

vicinity of C(2) together with the hydrogen atom H(7) for some time, after which H(7) forces H(2) in the direction of C(3) at 391.6 fs, such that C(3) has two hydrogen atom H(2) and H(3) at  $t$  values above 392.0 fs. The other five hydrogen atoms represented by the black and gray lines, vibrate around the attached carbon atoms without undergoing transfer.

The relative  $\beta(i)$  coordinates of each hydrogen atom,  $i$ , along the same trajectory are also shown in Figure 3.4(b). The thick solid line shows the  $\beta(7)$  values for the angle between hydrogen H(7) and the six membered ring, while the dotted line indicates  $\beta(1)$ . In the initial structure,  $\beta(1)$  and  $\beta(7)$  are approximately  $-20^\circ$  and  $20^\circ$ , respectively. At  $t = 30$  fs,  $\beta(1)$  decreases and start to oscillate at approximately  $0^\circ$ , following which H(1) and H(2) are located in the same plane of the six membered ring. Over the same period,  $\beta(7)$  oscillates around a value of  $30^\circ$  until proton transfer takes place. In this time range, H(7) can locate at neither C(1) nor C(2). At approximately  $t = 200$  fs,  $\beta(2)$  starts to slowly oscillate between 0 and  $-30^\circ$ . Simultaneously,  $\beta(7)$  starts to slowly oscillate until the proton transfer from C(2) to C(3) takes place at approximately  $t = 400$ . Following this,  $\beta(3)$  starts to slowly oscillate together with  $\beta(2)$ . During this stage,  $\beta(7)$  starts to oscillate between  $-10$  to  $10^\circ$ , such that H(7) is almost completely contained in the plane of the six membered ring.

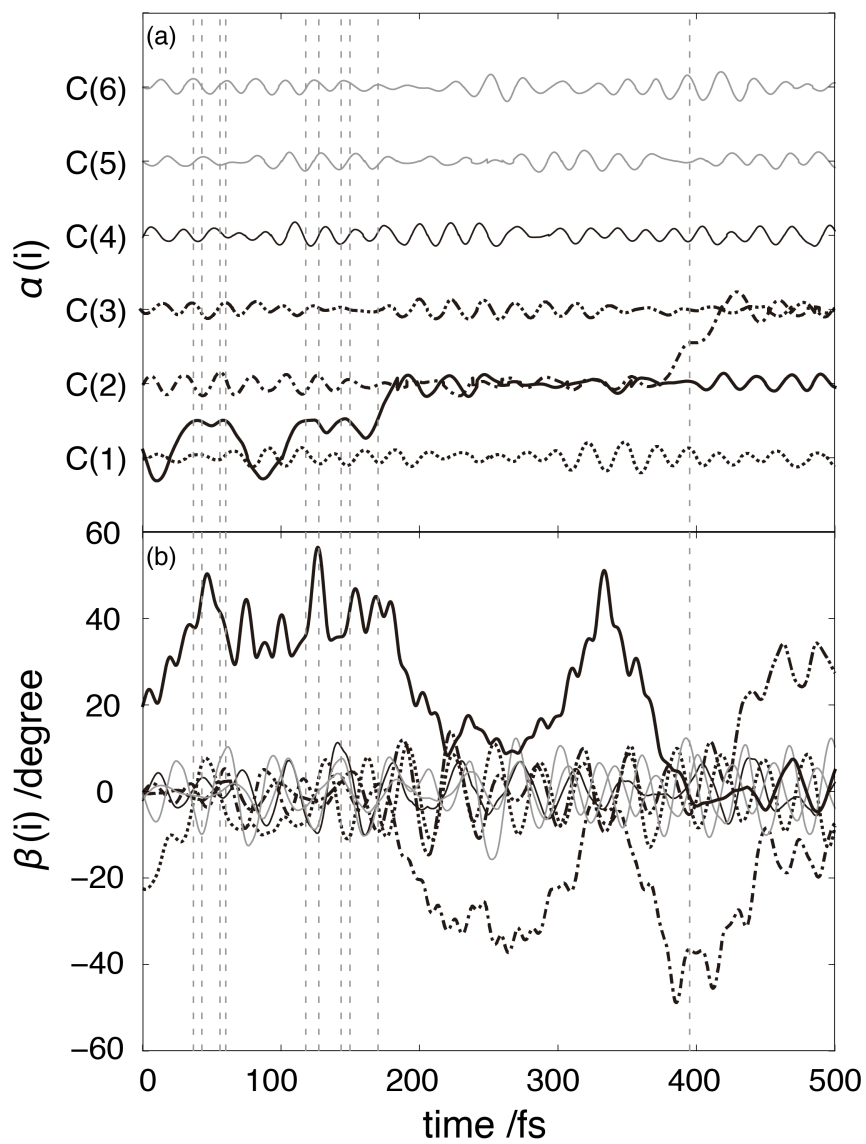


FIGURE 3.4: Relative coordinate through an example of trajectory. Index  $i$  points to the number of each atom.

### 3.5 Electronic states of the carbon atoms

I next examined the statistical distribution of  $\beta(i)$  for all hydrogen atoms ( $i = 1, \dots, 7$ ) only at the moment of proton transfers, as shown in Figure 3.5. The sharp peak at approximately  $\beta = 0^\circ$  corresponds to location of the hydrogen atoms almost exclusively on the six membered ring, while the two small peaks in the vicinities of  $\beta = \pm 40^\circ$  correspond to the transition state structure associate with proton transfer. At the moment of the proton transfer, the other six hydrogen atoms locate on the six membered ring and therefore there is no peak that corresponds to the stable position of  $sp^3$  protons (around  $\beta = \pm 20^\circ$ ) and the distribution is divided into three parts. The peak at a  $\beta$  value of approximately  $40^\circ$  is larger than the peak at  $-40^\circ$  because of the anti-symmetry of the initial conditions of the trajectories.

As noted, carbon atoms must change their orbital hybridization during proton transfers explained based on VB theory. As an example, in the initial structure, C(1) has  $sp^3$  hybrid orbitals while the remaining carbons have  $sp^2$  hybrid orbitals. The move of H(7) from C(1) to C(2) forces C(2) to generate  $sp^3$  hybrid orbitals and C(1) to change from  $sp^3$  to  $sp^2$  hybridization. In this manner, the carbon hybridizations reflect the position of the hydrogen atom. The peak at a  $\beta$  position of approximately  $0^\circ$  corresponds to  $sp^2$  hybridization, while the other values are assigned to  $sp^3$  hybrid orbitals. Here, I may roughly fit the peak at which  $\beta$  is approximately  $0^\circ$  with a normal distribution having a mean,  $\mu$ , of  $-1.25$  and a standard deviation,  $\sigma$ , of  $4.40$ . The

resulting normal distribution is indicated by the red line in Figure 3.5. In this work, I assume that a carbon atom has formed  $sp^2$  hybrid orbitals when the following hold true:

$$\mu - 2\sigma \leq \beta \leq \mu + 2\sigma . \quad (3.5)$$

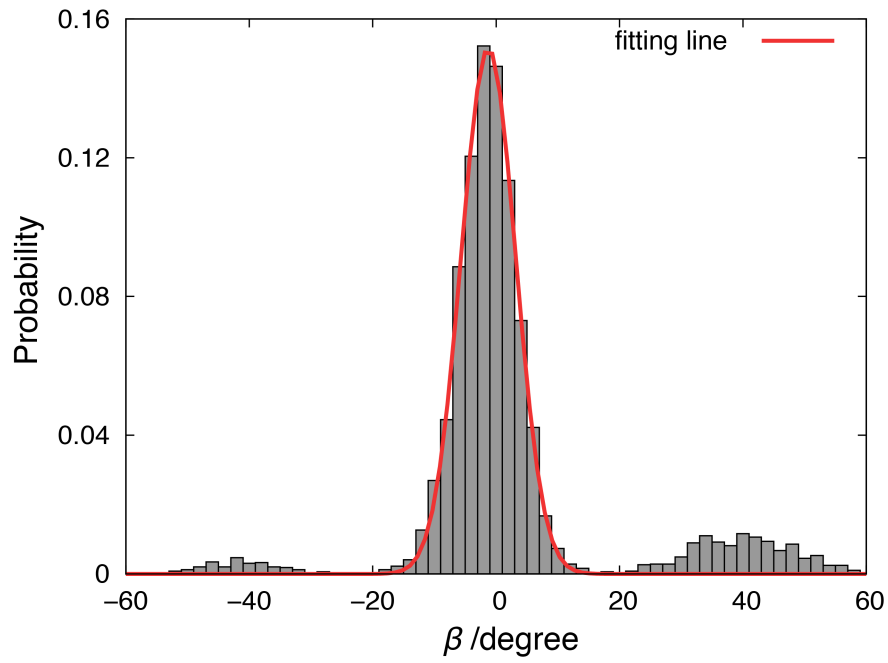


FIGURE 3.5: Histogram of  $\beta$  with the fitting line by standard distribution.

### 3.6 Electronic states for non-statistical lifetime distribution

Based on the above discussions, the relative coordinate,  $\beta$ , can be used to judge the electronic states of carbon atoms, specifically whether they possess  $sp^2$  or  $sp^3$  hybrid orbitals. The histogram of  $\alpha(i)$  values for the transferred proton is presented in Figure 3.6. As noted above,  $\alpha(i)$  values of approximately 1 or 0 indicates that the proton is located on the carbon atom. Figure 3.6 shows that the proton usually locates near carbon atoms. It is interesting to note that these data indicates that the contribution at an  $\alpha(i)$  value of 0.5 is rather large. This figure therefore demonstrates that there are many trajectories for which the proton becomes trapped in the transition state region.

To analyze the nature of the short lifetime proton transfer, I also examined the hybridization of proton donor and acceptor carbon atoms. There are four possible combinations of hybridization of two carbon atoms:  $(sp^3, sp^3)$ ,  $(sp^3, sp^2)$ ,  $(sp^2, sp^2)$  and  $(sp^2, sp^3)$ . In this notation, the first and second hybridization indicate the electronic structures of the donor and acceptor carbons, respectively. The histogram in Figure 3.6 is divided into the 4 cases and these are further represented in Figures 3.7(a) – (d), showing  $(sp^3, sp^2)$ ,  $(sp^2, sp^2)$ ,  $(sp^3, sp^3)$ , and  $(sp^2, sp^3)$  in panels (a), (b), (c) and (d), respectively. The most frequent combination is seen to be  $(sp^3, sp^2)$  in Figure 3.7(a).

Here I focus on the significant case of  $(sp^2, sp^3)$  hybridization, as shown in Figure 3.7 (b), which

shows a wide range of  $\alpha$ . It is evident that there are numerous components at an  $\alpha$  value of approximately 0.5, in contrast to Figures 7(a), (c) and (d). I consider that these plots include the effects of proton-trapped states lasting for tens of femtoseconds. That is, the transferred proton is trapped and oscillates in the transition state because both adjacent carbon atoms form  $sp^2$  hybrid orbitals and thus the proton can locate on neither atom. Such electronic states occurring in the dynamic process could cause the non-statistical lifetime distributions found for the proton transfer reaction.

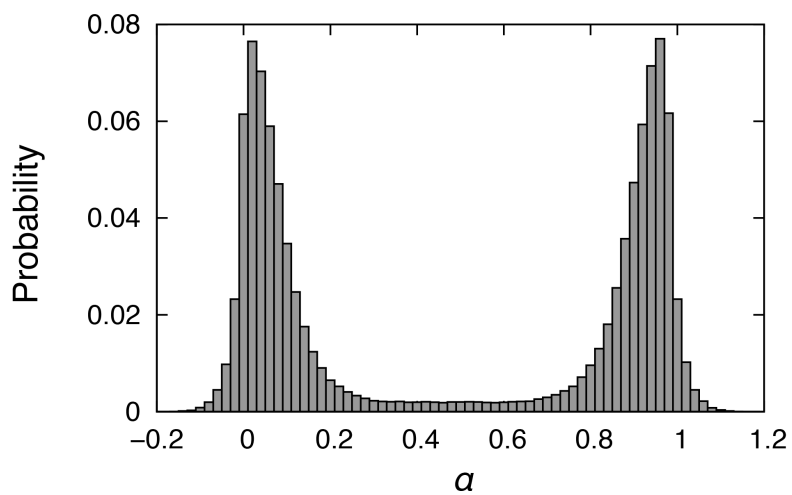


FIGURE 3.6: Histogram for relative coordinate  $\alpha$  from transferred proton in all trajectories

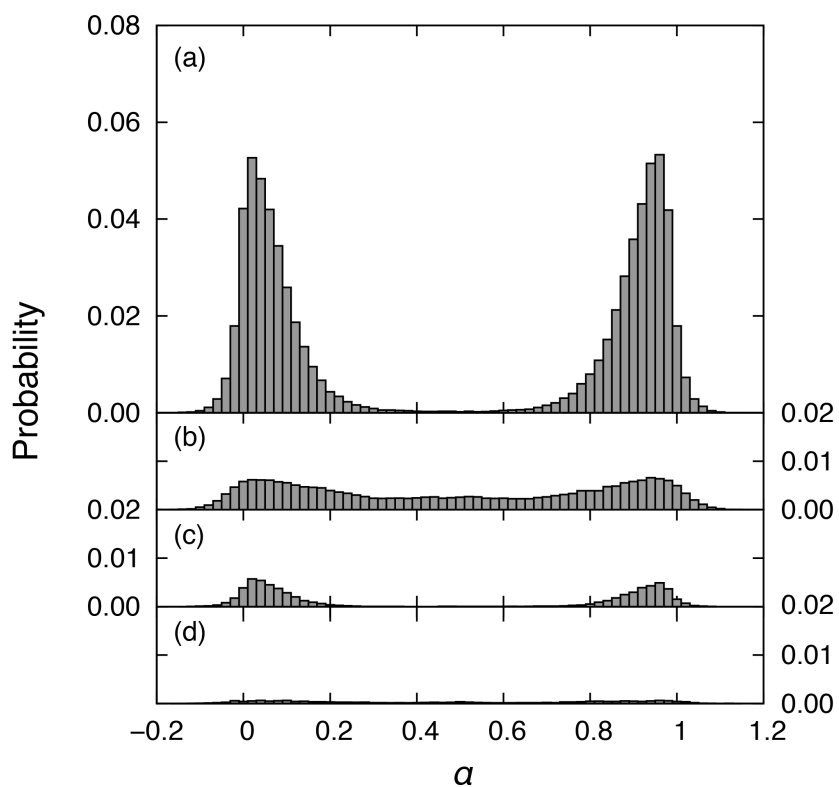


FIGURE 3.7: Histogram for relative coordinate  $\alpha$  from transferred proton in all trajectories, divided into (a)( $sp^3, sp^2$ ), (b)( $sp^2, sp^2$ ), (c)( $sp^3, sp^3$ ), and (d)( $sp^2, sp^3$ ) by Equation (3.5)

### 3.7 Conclusions

I analyzed the mechanism of the proton transfer reaction in protonated benzene using *ab initio* molecular dynamics simulations. The lifetime distribution calculated from the trajectories exhibits non-statistical behavior, since it includes a large number of short lifetime trajectories. In order to investigate the nature of these short lifetime trajectories, I introduced the concept of a relative coordinate,  $\alpha$ , and a vertical direction,  $\beta$ . Using these coordinates, I found that both carbon atoms adjacent to the transferred proton form  $sp^2$  hybrid orbitals during the exchange and that the transferred proton is trapped and oscillates between the two carbon atoms for a period of several several dozen femtoseconds. The proton is therefore held between the two carbons, leading to the frequent appearance of short lifetime reactions. The remarkable phenomenon is believed to be a common occurrence associated with proton transfer reactions accompanied by changes in orbital hybridization.



## Chapter 4

# Ammonia borane dehydrogenation

### 4.1 Ammonia borane dehydrogenation reaction for H<sub>2</sub> storage

Ammonia borane (AB = NH<sub>3</sub>BH<sub>3</sub>), a molecule first prepared by Shore and Parry in 1955 [36], has been studied extensively in recent years, chiefly due to its potential to be utilized as a chemical hydrogen-storage material. Although releasing H<sub>2</sub> from AB takes place thermally without a catalyst, high temperatures and slow reaction rates are the main drawbacks to use of AB as a carrier for hydrogen. In contrast, metal-catalyzed release of H<sub>2</sub> from AB could operate at a lower temperature and produce H<sub>2</sub> at a much faster rate. Furthermore the extent of H<sub>2</sub> released could be higher in a metal-catalyzed process, owing to the high gravimetric capacity of hydrogen in AB (19.6 wt %). Driven by these benefits, sufficient efforts have been made to develop catalytic systems for AB dehydrogenation.

The first transition metal catalyst for the dehydrogenation of AB, (POCOP)Ir(H)<sub>2</sub> (POCOP = [*h*<sup>3</sup>-1,3-(OPtBu<sub>2</sub>)<sub>2</sub>C<sub>6</sub>H<sub>3</sub>]), was reported in 2006 by Goldberg et al [37]. Since effective homogeneous catalysts for alkane dehydrogenation had been reported and amineboranes are

isoelectronic with alkanes, they conceived the application of such complexes to the problem of amineborane dehydrogenation.

As the by-product  $(\text{BN})_n$  generated by 3 equiv. of  $\text{H}_2$  released is insoluble and inactive, it is not suitable for regenerating the reactant AB. Baker et al. described that there needs to be controlled the two fundamental reaction pathways shown in Scheme 4.1 for the effective catalysts for AB dehydrogenation [38]. In some cases, insoluble  $(\text{NH}_2\text{BH}_2)_n$  is generated with rapid release of a single equiv of  $\text{H}_2$  (lower pathway, Scheme 4.1). Several catalysts, however, can release greater than 2 equiv of  $\text{H}_2$  per molecule of AB [39]–[42]. For the large amounts of dehydrogenation, trapping of AB in the form of  $\text{Cy}_2\text{BNH}_2$  (Cy = cyclohexyl) is suggested to release efficient of  $\text{NH}_2\text{BH}_2$  (upper pathway, Scheme 4.1), which affords borazine and polyboradilene. Moreover, polyboradilene can regenerate AB nearly quantitatively by 24 h treatment with hydrazine ( $\text{N}_2\text{H}_4$ ) in liquid ammonia at  $40^\circ\text{C}$  [43].

These dehydrogenation catalysts often involve trace metal. Therefore, iron-based catalytic systems would be even more desirable because iron is relatively inexpensive and the most abundant transition metal. In recent study by Bhattacharya et al, a series of iron bis(phosphinite) pincer complexes are found to catalyze dehydrogenation of AB [44]. The complexes,  $[\text{2,6-}(\text{iPr}_2\text{PO})_2\text{C}_6\text{H}_3]\text{Fe}(\text{PMe}_2\text{R})_2\text{H}$  (R = Me, shown in Figure 4.1(a); R = Ph, (b)) and  $[\text{2,6-}(\text{iPr}_2\text{PO})_2\text{-4-(MeO)C}_6\text{H}_2]\text{Fe}(\text{PMe}_2\text{Ph})_2\text{H}$  (c) can afford to release 2.3-2.5 equiv of  $\text{H}_2$  per AB

in 24 h. Among the three catalysts, the complex given in Figure 4.1 (c) exhibits the highest activity, followed in order by (b) and (a). The proposed catalytic cycle is shown in Scheme 4.2.

The rate-determining step involves breaking the N-H and B-H bonds of AB, which results in the protonation of *ipso* carbon and the transfer of a hydride ligand from boron to iron. Alternative mechanisms without the protonation of the *ipso* carbon seem to be less likely.

In this study, I verify the proposed reaction cycle and determine the cause of the difference of the catalytic activity by examining the influences of ligands.

SCHEME 4.1: Reaction pathways lead to different AB dehydrogenation products

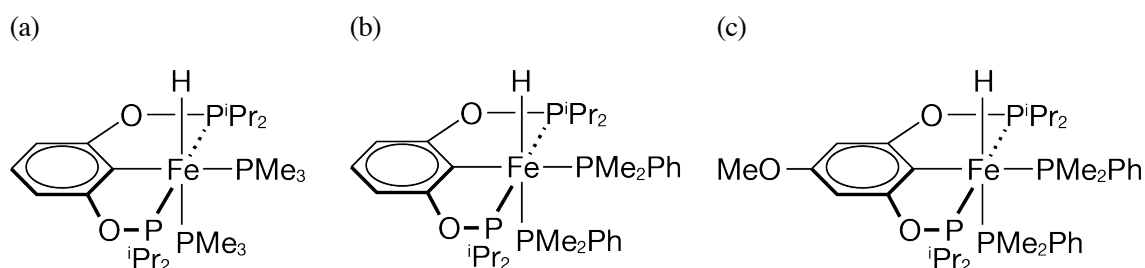
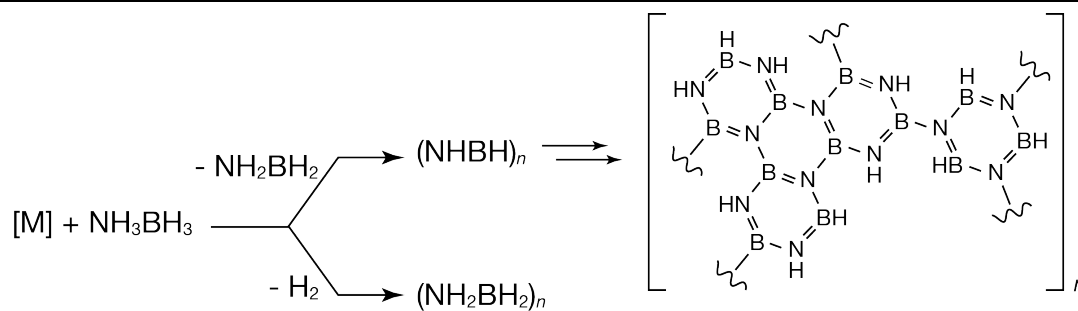


FIGURE 4.1: Iron POCOP-pincer complexes

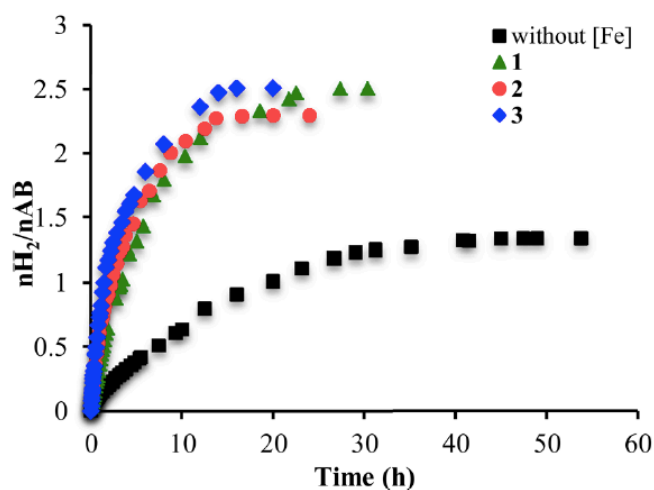
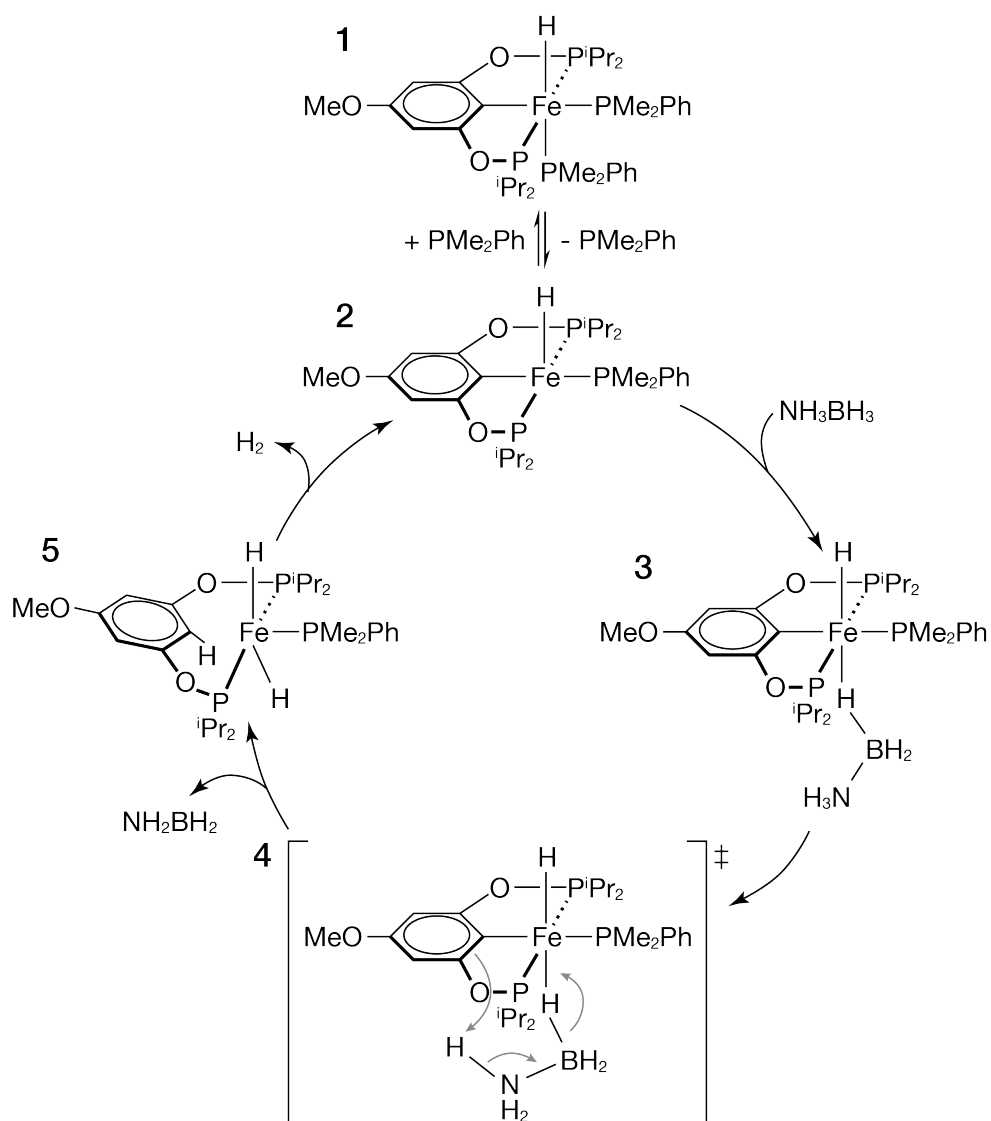


FIGURE 4.2: Amount of H<sub>2</sub> released from AB (1.0 M solution in 1:4 THF/diglyme) at 60 °C with or without an iron catalyst (5 mol %)[44]. The legends 1, 2 and 3 correspond to (a), (b) and (c) in Figure 4.1, respectively.

SCHEME 4.2: Catalytic cycle for the dehydrogenation of AB catalyzed by (c) proposed in ref [44].



## 4.2 Calculation methods

I optimized all the molecular geometries by using the hybrid meta exchange-correlation M06 methods [45]–[47], which is able to describe noncovalent interactions. These calculations were performed with tight convergence criteria and pruned fine grids. The effective core potentials (ECPs) of Hay and Wadt with double- $\zeta$  valence basis sets (LanL2DZ) were applied to describe the iron [48][49]. Moreover polarization functions were added for Fe ( $\zeta_f = 2.462$ ) [50][51]. The 6-31G(d,p) basis set was used for all the other atoms, C, H, B, N, O and P. Frequency of each geometry were calculated to verify all stationary points and transition states, while to provide Gibbs free energies at 298.15 K. All calculations were performed using the Gaussian 09 software package [63].

To replace the large isopropyl groups with more small substituents in the POCOP-pincer ligands of each species, I compared the Mulliken charges [52] and natural charges [13] of Fe and four P atoms in the test system in Figure 4.3 that of R substituents replaced with H, methyl group, and originally isopropyl group. As shown in Table 4.1 and 4.2, both Mulliken and natural charges of R = Me compounds are close value to those of R = <sup>i</sup>Pr compounds. Therefore I replace the isopropyl groups to methyl groups in all the compounds in this study.

The series of complexes given in Figure 4.1 (a) to (c) which isopropyl groups replaced to methyl groups refer to A, B and C respectively.



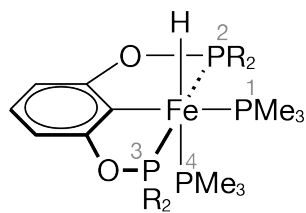


FIGURE 4.3: Labels of atoms in test system

TABLE 4.1: Mulliken charge of iron and phosphorus

	Fe	P1	P2	P3	P4
R = H	-1.6931	0.7163	0.8706	0.8815	0.6815
R = Me	-1.9184	0.7384	1.1023	1.0869	0.7516
R = iPr	-2.1066	0.7685	1.2176	1.2029	0.8168

TABLE 4.2: Natural charge of iron and phosphorus

	Fe	P1	P2	P3	P4
R = H	-2.1817	1.3703	1.1648	1.1711	1.3533
R = Me	-2.1225	1.3643	1.7126	1.7086	1.3475
R = iPr	-2.0388	1.3488	1.7143	1.6859	1.3272

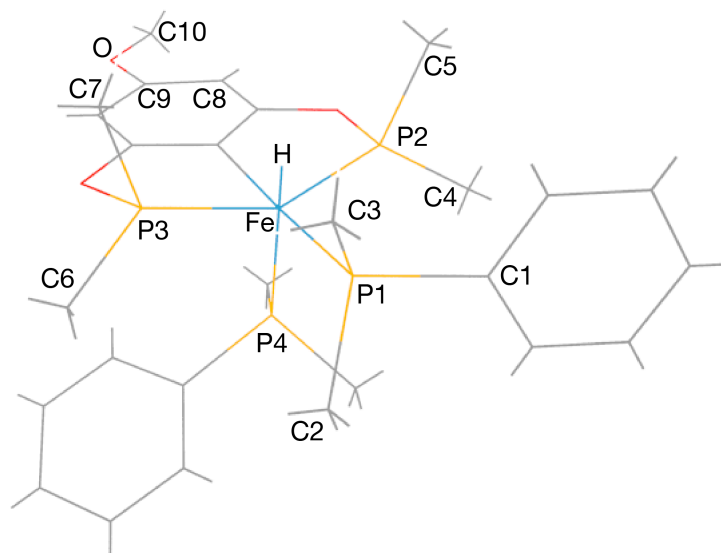
### 4.3 Electronic states and influence of the phenyl group

The rotation of  $\text{PMe}_3$  and  $\text{PMe}_2\text{Ph}$  ligands highly effects on the potential energy. In order to optimize the each step of most stable structures, I scanned the potential energy curves of structure 2, 3 and 5 described by the torsion angle  $\theta(\text{H-Fe-P1-C1})$  by 10-degree interval for each torsion while the other degrees of freedom were optimized (Figure 4.5-4.7). As is shown in Figure 4.4, H is the hydride on iron atom, and C1 is the carbon in phenyl group and next to the phosphine atom. Since the  $\text{PMe}_3$  and  $\text{PMe}_2\text{Ph}$  substituents have C-3 and C-2 axes of symmetry each other, only from 0 to 120 degree of the A and from 0 to 180 degree of the B and C were calculated and reflected the values from the bigger angle to 360 degree. All the energy were relative to the structure of  $\theta(\text{H-Fe-P1-C1}) = 0$ .

The torsion angles  $\theta(\text{H-Fe-P1-C1})$  in the minimum energy conformations of A-2 are 60, 180 and 300 degrees because of its  $C_3$  symmetry. Similarly,  $\theta(\text{H-Fe-P1-C1})$  of 60 and 120 degrees provide minimum energy in the case of B-2, 300 degree in C-2, 0, 60, 180 and 300 degrees in A-3 (very small energy differences), 120 and 240 degrees in B-3, 240 degree in C-3, 0, 120 and 240 degrees in A-5, 120 and 240 degrees in B-5, and 240 degree in C-5. Regardless of the substituents, the species of compounds 2 and 5 make the same torsion angle correspond to the minimum energy, while A-3 has different values from B-3 and C-3. Furthermore, the same angle of 3 and 5 in complex B and C were formed in the minimum energy, conformations.

Therefore the transition states, B-4 and C-4, are presumed that the structure 4 forms the minimum energy structure at the same angle each other. Then, the initial state of the 4 were set to  $\theta(\text{H-Fe-P1-C1}) = 240$  degree.

On the other hand, compounds C have methoxy (OMe) group on the para position of the POCOP phenyl ring. In the same way as finding the most stable state of OMe, I scanned the potential energy curves of C-2, C-3 and C-5 described by the torsion angle  $\phi(\text{C8-C9-O-C10})$  by 10-degree interval for each torsion while the other degrees of freedom were optimized. As shown in Figure 4.8, C-2 and C-5 form 0 degree of  $\phi(\text{C8-C9-O-C10})$  and C-3 forms -10 degree at the minimum energy, while the difference is slight.



---

FIGURE 4.4: Example of labels on atoms in C-1 structure

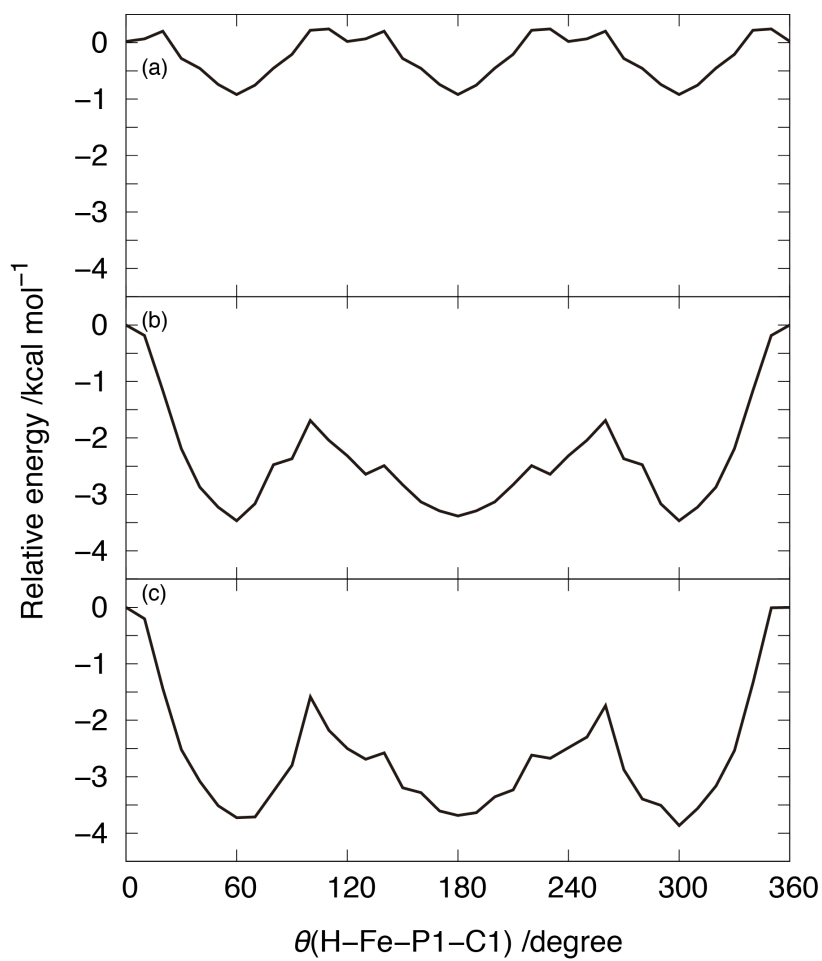


FIGURE 4.5: Effect of torsion angle  $\theta(\text{H-Fe-P1-C1})$  on the energy of structure 2 of (a) complex A, (b) complex B and (c) complex C. All the energies are relative to  $\theta(\text{H-Fe-P1-C1}) = 0$ .

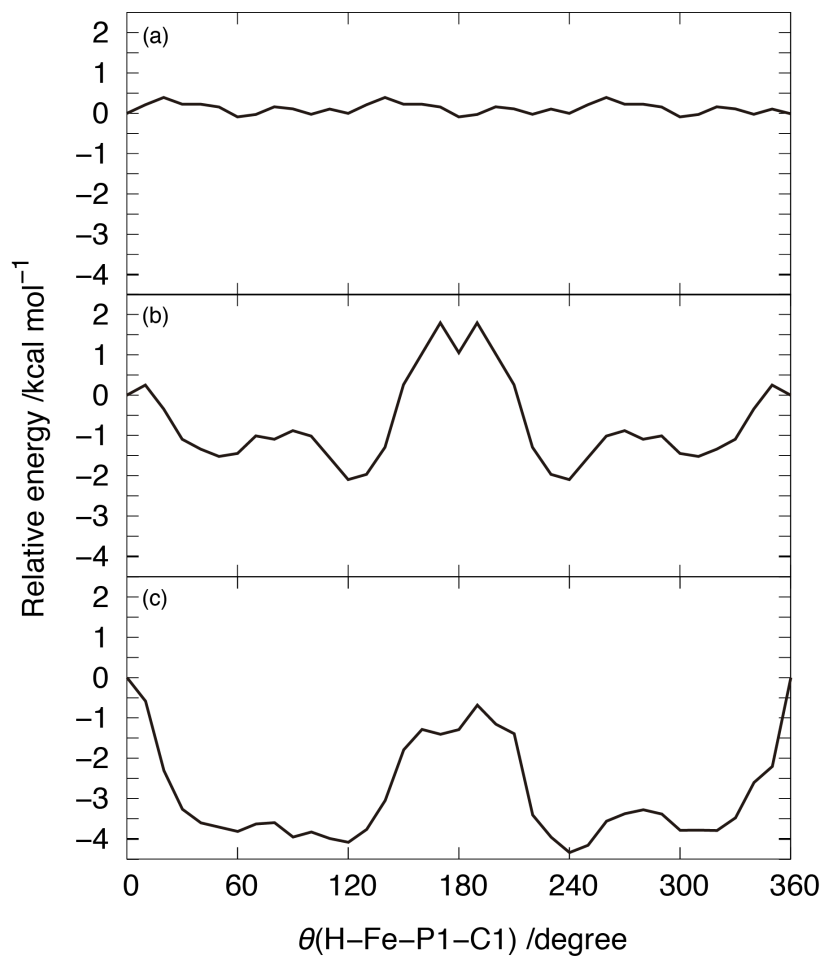


FIGURE 4.6: Effect of torsion angle  $\theta(\text{H-Fe-P1-C1})$  on the energy of structure 3 of (a) complex A, (b) complex B and (c) complex C. All the energies are relative to  $\theta(\text{H-Fe-P1-C1}) = 0$ .

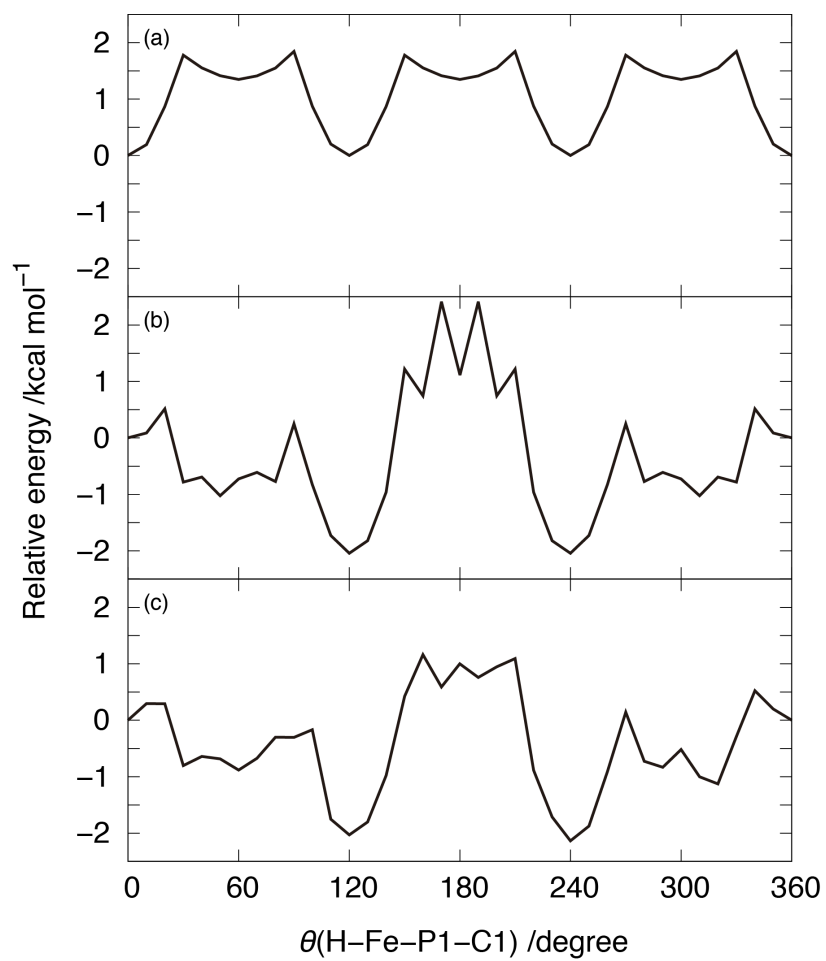


FIGURE 4.7: Effect of torsion angle  $\theta(\text{H-Fe-P1-C1})$  on the energy of structure 5 of (a) complex A, (b) complex B and (c) complex C. All the energies are relative to  $\theta(\text{H-Fe-P1-C1}) = 0$ .

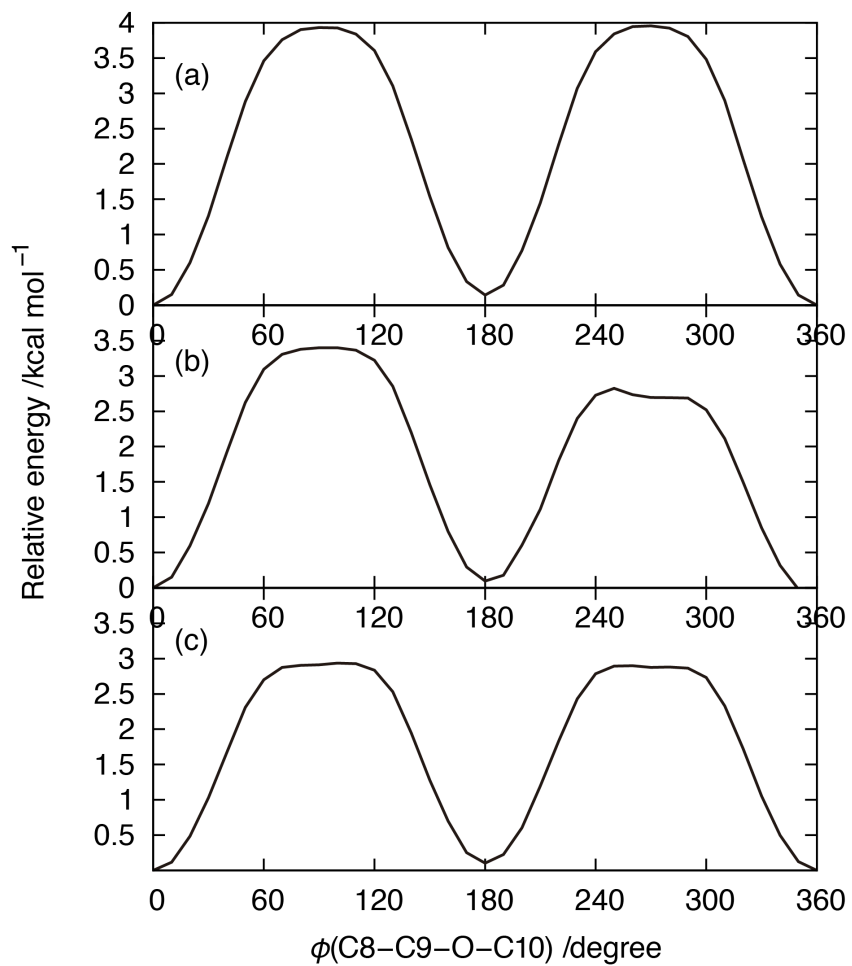


FIGURE 4.8: Effect of torsion angle  $\phi(\text{C8-C9-O-C10})$  on the energy of structure of (a) C-2, (b) C-3 and (c) C-5. All the energies are relative to  $\phi(\text{C8-C9-O-C10}) = 0$ .

#### 4.4 Energy profiles of the reaction cycle

The Gibbs energies ( $\Delta G$ ) based on M06 energies with Gibbs energy corrections (at 298.15 K) and solvation corrections is shown in Figure 4.9. The polarizable continuum model (PCM) was used for solvation effect [53]–[55]. In this model, the solvent is specified by its dielectric constant. THF- $d_8$ /diglyme was used in the experiments by Bhattacharya et al. On the other hand, the dielectric constants of diglyme is approximately equal to that of THF (diglyme: 7.20~7.58, THF: 7.58) [56]. Therefore THF is specified for my PCM calculation.

In consideration of the result of the effect of trimethylphosphine ( $\text{PMe}_3$ ) and dimethylphenylphosphine ( $\text{PMe}_2\text{Ph}$ ) torsion on the energy, the global minimum conformations of 2, 3 and 5 are found. 5 has the global minimum at almost the same angle with 3. This result suggests that the transition state 4 also forms the same angle with 3 and 5.

Shown in Figure 4.9, the rate-determining step in A is hydride and proton transfer (from 3 to 5), while the activation energies in B and C are not so high. It corresponds to the experimental results of dehydrogenation activities [44]. As seen the process of the hydride and proton transfer reaction, the activation barrier for the reaction is lowered by  $\text{PMe}_2\text{Ph}$  ligand in comparison with  $\text{PMe}_3$  ligand. The reason is explained in section 4.5. The intermediates 5, after  $\text{NH}_2\text{BH}_2$  released, are not the proposed *ipso* carbon protonation structure but dihydrogen complexes [57].

On the other hand, I scanned the potential energy curves of structure A-1, B-1 and C-1

described by the atomic distance  $r(\text{Fe-P4})$  by 0.2 Å interval from the each stable structure while the other degrees of freedom were fixed (Figure 4.10). It shows that there is no barrier in the release process of  $\text{PMe}_3$  or  $\text{PMe}_2\text{Ph}$  substituents opposite to hydride (from the structure 1 to 2) in each complex. Although the energy difference is bigger than the activation energy in B and C complexes each other, it is not related the catalytic cycle if once the substituents are released. The difference of Gibbs free energies between  $\text{NH}_3\text{BH}_3$  and sum of  $\text{NH}_2\text{BH}_2$  and  $\text{H}_2$  is -6.27 kcal mol<sup>-1</sup>. It is assumed that the dehydrogenation of ammonia borane is exothermic reaction.

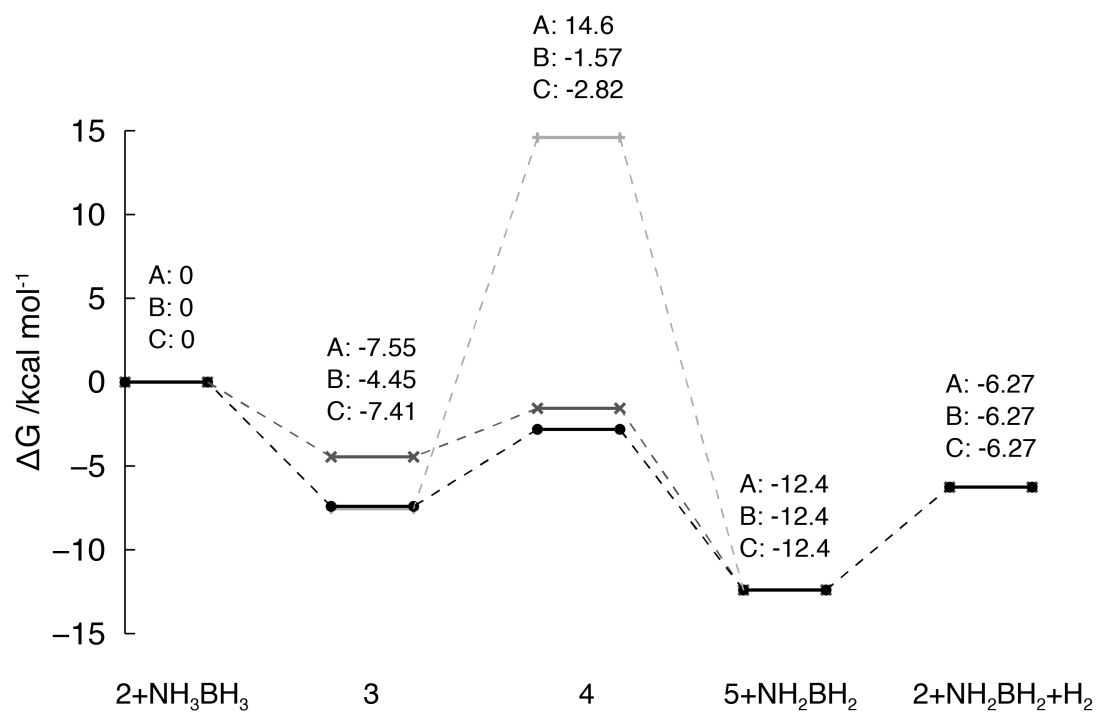


FIGURE 4.9: Potential energy profile of the dehydrogenation of AB catalyzed by POCOP-pincer Fe complexes.

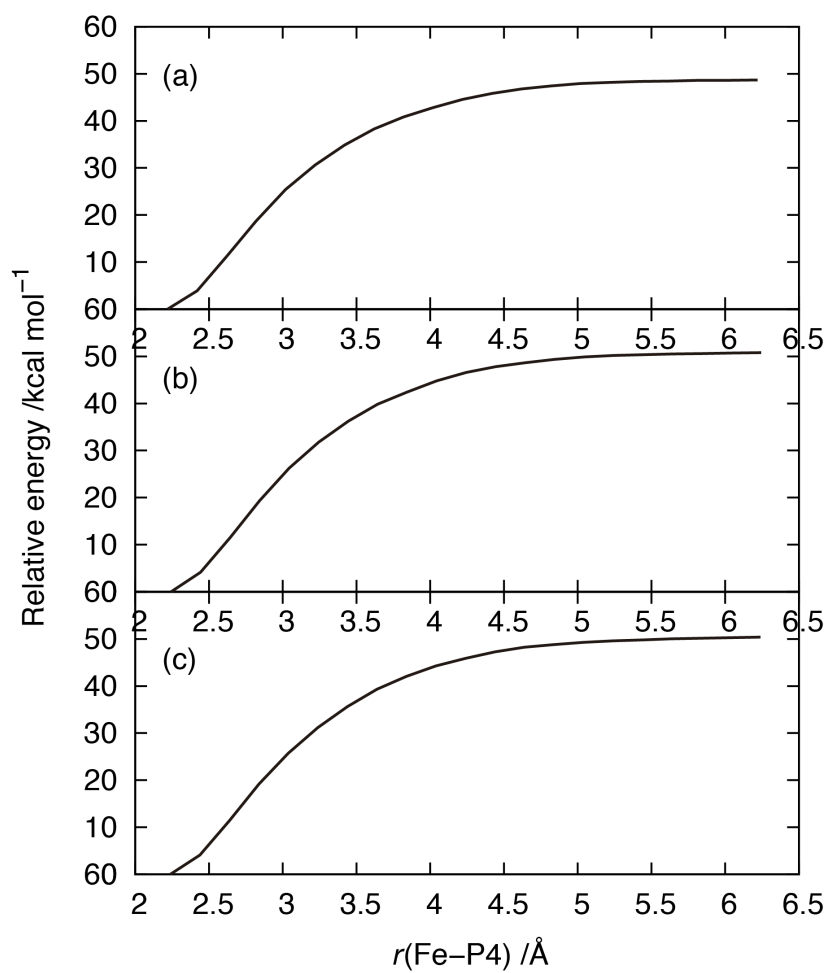


FIGURE 4.10: Effect of atomic distance  $r(\text{Fe-P4})$  on the energy of structure of (a) A-1 (b) B-1 and (c) C-1. All the energies are relative to each stable state.

## 4.5 Reactivity difference among the $\text{PMe}_3$ and $\text{PMe}_2\text{Ph}$ groups

I calculated the natural charge of each methyl and phenyl group and represented in Table 4.3.

For example, Me1 is methyl group including C1 in Figure 4.12 (as for other substituents of same labels). Compared with the values of A-4, the phenyl group in B-4 has large amount of electron. Since all the substituents have negative charge, repulsive forces are generated among themselves.

The repulsion between Ph1 and Me4, instead of isopropyl group in my calculation, is reflected the relative coordinate. According to the interatomic distance in Table 4.4, the distance between the boron atom in  $\text{NH}_3\text{BH}_3$  and C4 included in Me4 is 3.875 Å in B-4 whereas 3.800 Å in A-4. The distance Fe-P2 is also extended in B-4. Consequently,  $\text{PMe}_2\text{Ph}$  group expands space capable of being attached by  $\text{NH}_3\text{BH}_3$ .

Here I confirm the dehydrogenation mechanism of AB.  $\text{NH}_3\text{BH}_3$  and  $\text{NH}_2\text{BH}_2$  are isoelectronic with  $\text{CH}_3\text{CH}_3$  and  $\text{CH}_2\text{CH}_2$  each other. The optimized structure of AB and  $\text{NH}_2\text{BH}_2$  are shown in Figure 4.11. In the case of ethane,  $\text{sp}^3$  to  $\text{sp}^2$  transformation is occurred with the release of  $\text{H}_2$  and ethene is generated. Similarly,  $\text{H}_2$  elimination from AB causes the change of hybridization from  $\text{sp}^3$  to  $\text{sp}^2$ , and boron-nitrogen bonding becomes like a double bond. By the way, I explained that  $\text{sp}^2$  hybrid orbital formed in carbon atoms rejects transferred proton in Chapter 3. In other words, the more capable of being  $\text{sp}^2$  hybrid orbital of B-N bond, the more released

proton. Larger space around AB would make  $\text{NH}_2\text{BH}_2$  possible to be planar structure and lower the activation barrier of dehydrogenation. Therefore  $\text{PMe}_2\text{Ph}$  instead of  $\text{PMe}_3$  on Fe enhances catalytic activity.

Moreover the torsion angle of 2 in the global minimum structure is different from that of 3 and 5 as mentioned in the section 4.3. It can be regarded that each structure of 4 forms almost the same torsion angle with 3 and 5. As plotted the relative energy and boron-nitrogen bond length  $r(\text{B-N})$  of A-3 and B-3 against torsion angle  $\theta(\text{H-Fe-P1-C1})$  in Figure 4.13 and 4.14, the potential energy becomes minimum when the B-N bond is almost shortest. Therefore  $\text{PMe}_2\text{Ph}$  ligand rotates in the process from the structure 2 to 3, while the distance  $r(\text{B-N})$  is shortened. The boron and nitrogen form  $\text{sp}^2$  hybridization, and they can release proton and hydride.

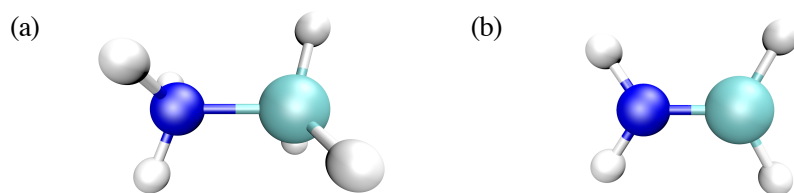


FIGURE 4.11: Optimized structure of (a)  $\text{NH}_3\text{BH}_3$  and (b)  $\text{NH}_2\text{BH}_2$  obtained in the M06/6-31G(d,p) calculation

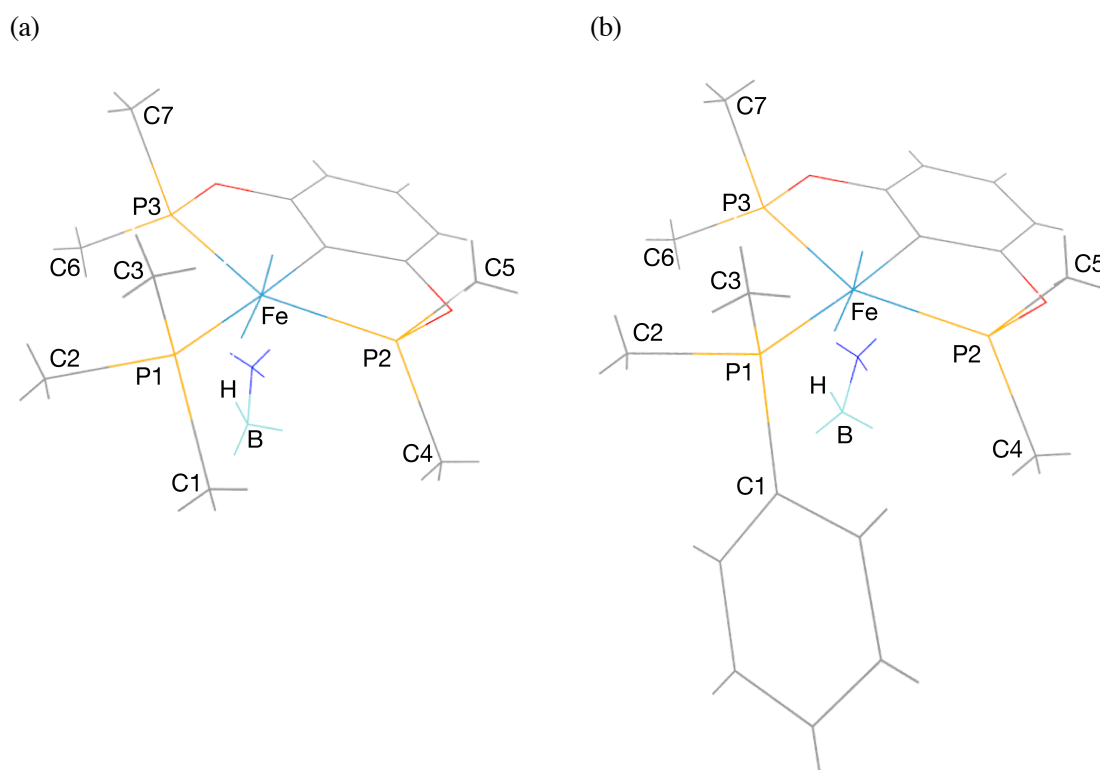


FIGURE 4.12: Labels of atoms in (a) A-4 and (b) B-4 structures

TABLE 4.3: Natural charge of methyl and phenyl groups

	A-4	B-4
Me1 (Ph1)	-0.2753	-0.3226
Me2	-0.2803	-0.2731
Me3	-0.2560	-0.2577
Me4	-0.2802	-0.2714
Me5	-0.2857	-0.2844
Me6	-0.2981	-0.2926
Me7	-0.2801	-0.2795

TABLE 4.4: Interatomic distances (Å)

	A-4	B-4
B-C4	3.800	3.875
Fe-P1	2.186	2.195
Fe-P2	2.149	2.164
Fe-P3	2.130	2.135
Fe-H	1.727	1.732
H-B	1.270	1.245
Fe-B	2.810	2.806

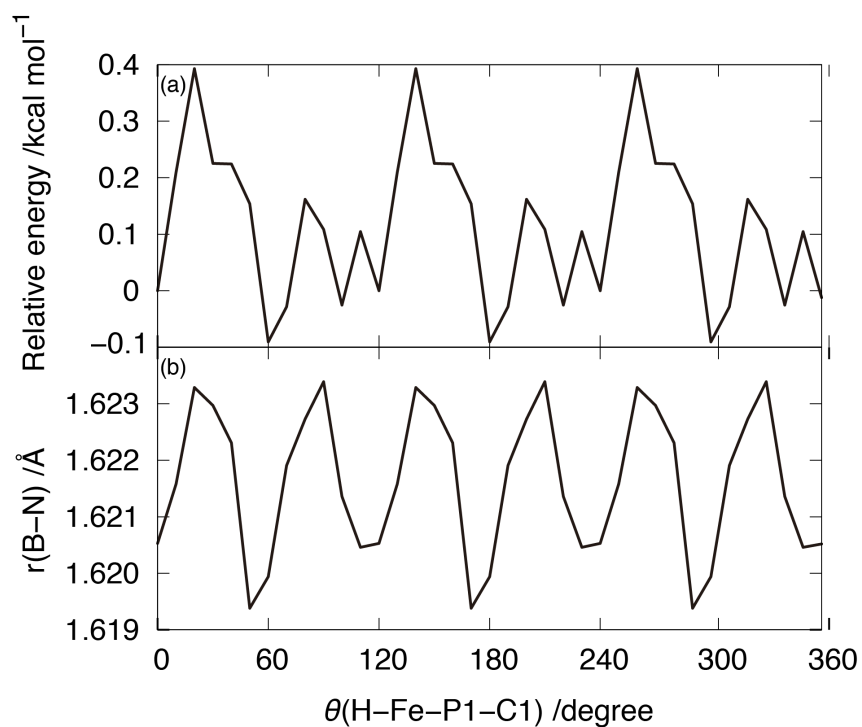


FIGURE 4.13: Relative energy (a) and boron-nitrogen bond length (b) of trimethylphosphine rotation in A-3 in the range of the torsion angle from 0 to 360°

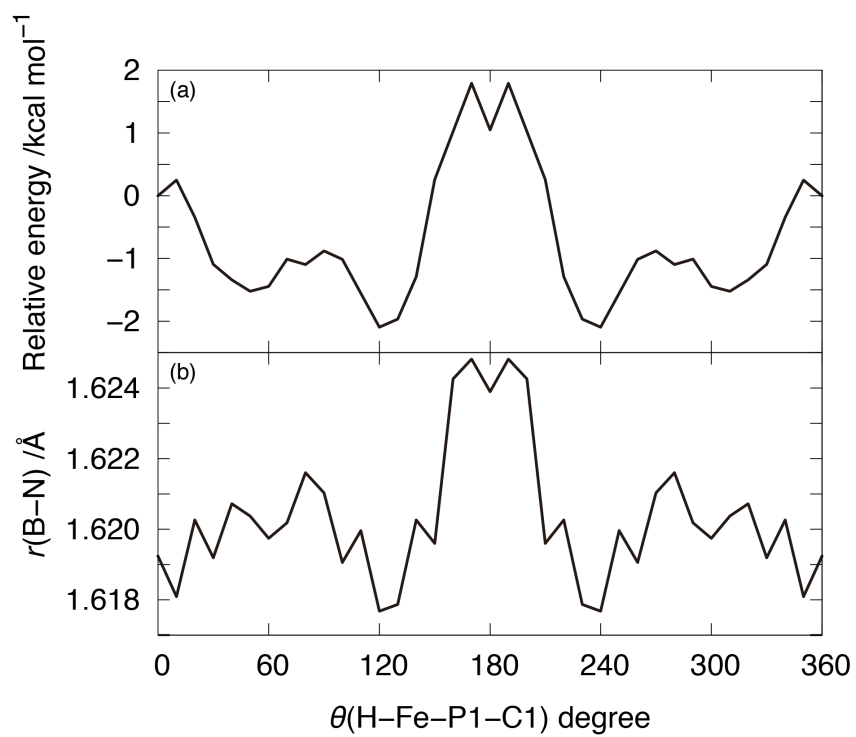


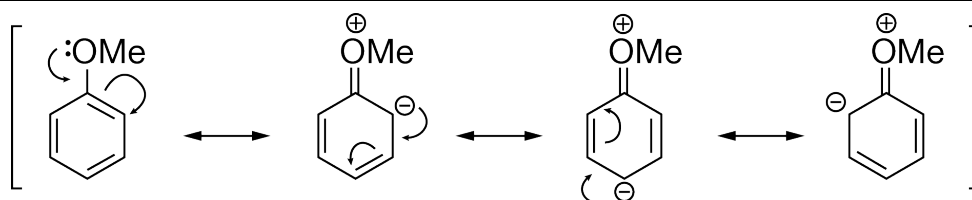
FIGURE 4.14: Relative energy (a) and boron-nitrogen bond length (b) of dimethylphenylphosphine rotation in B-3 in the range of the torsion angle from 0 to 360°

## 4.6 Electron-donating by the OMe group

The difference between B and C is the existence of the *p*-methoxy group on the POCOP phenyl group. From the energy diagram given in Figure 4.9, the methoxy group stabilizes particularly structure C-3 and C-4.

Generally, it is known that methoxy group on aromatic compounds exhibits electron donation properties because of the donor-acceptor (resonance) interactions of the lone electron pairs of the O atom with the antibonding  $\pi^*$  orbitals of the benzene ring shown in Scheme 4.3 [58]. The both key steps,  $\text{PMe}_2\text{Ph}$  elimination (from 1 to 2) and the hydride and proton transport (from 3 to 5) would be favorable by electron supplied to iron. Therefore methoxy group promotes the reaction process.

SCHEME 4.3: Electronic resonance interaction on methoxy group



## 4.7 Conclusions

The dehydrogenation mechanisms of the ammonia borane ( $\text{NH}_3\text{BH}_3$ , AB) molecule with Fe POCOP-pincer catalysts have been investigated through DFT calculations. By the energy diagram calculation, it was revealed that the rate-determining step in A is hydride and proton transfer, while that in B and C does not take high energy in the proton and hydride transfer. By addition of AB to 2,  $\text{PMe}_2\text{Ph}$  group is rotated. The negative bulky  $\text{PMe}_2\text{Ph}$  ligand repels neighbor methyl group, then it causes AB easy to form hybridization from staggered conformer to planar  $\text{NH}_2\text{BH}_2$  by released proton and hydride. Due to the rotation of  $\text{PMe}_2\text{Ph}$  group, the B-N bonding would be shorter and it stabilizes the complex. At the same moment,  $\text{NH}_2\text{BH}_2$  is liable to eliminate. It is equal to hydride and proton transport to the catalyst. In this way, the intermediates and transition states of B and C in hydride and proton transfer reaction is stabilized and the activation barriers would be lower.

On the other hand, the *p*-methoxy group on aromatic ring is electron-donating group because of the resonance interactions of the lone pairs of the oxygen atom with the antibonding  $\pi^*$  orbitals of the aromatic ring. The interactions by the methoxy group more stabilize the each compound of C, including C-2 which forms the highest potential barrier.



## Chapter 5

### Discussion

VB theory assumes that all bonds are localized bonds formed between two atoms by the donation of an electron from each atom. It corresponds to geometry, therefore can explain the electronic states and bonding for whatever stable states.

In the similar manner of Bader's Atoms in Molecules theory, that defines the bonding based on electron density, I set  $sp^2$  and  $sp^3$  hybridization from MD trajectories by VB theory, and examined the relationship between the change of hybridization and intramolecular proton transfer in protonated benzene. In this molecule, I elucidated that the reaction path is controlled by the transformation between  $sp^3$  and  $sp^2$  hybridization of carbon atoms and adjacent two  $sp^2$  hybrid orbitals do not allow the proton to make a bond with them. In the case of the proton transfer in dioxonium ion mentioned in chapter 1, the barrier height is dependent on the oxygen-oxygen distance. The activation energy in protonated benzene is not so much determined by the carbon-carbon distances as the hydrogen vibrational modes perpendicular to benzene ring, which are closely related to the hybridization of carbons.

These phenomena are said to enhance the tunnel effect together with the quantum effect of hydrogen. They appeared in the lifetime distribution as short lifetime reactions.

Protonated benzene has carbon-carbon bonds, while ammonia borane has boron-nitrogen bond.

Ammonia borane is isoelectronic with ethane, hence boron-nitrogen bond also transforms with  $H_2$  released in the same way of dehydrogenation in ethane. When the transformation of hybridization occurs,  $sp^2$  hybridizations on boron and nitrogen are expected to repel and release the hydrogens. For this reason, the activation barrier of proton transfer may be lowered by the  $sp^2$  hybridization easy to form.

POCOP pincer ligand makes covalent bond between benzene ring and transition metal. The robust structure stabilizes the complex and prevents to be broken the catalyst through the reaction cycle. In my calculated systems, higher reactive catalysts have the  $PMe_2Ph$  ligand. The ligand rotates and the phenyl group gets close to the attached ammonia borane in spite of the high bulkiness. The phenyl group does not have steric hindrance. The  $PMe_2Ph$  ligand repels neighbor trimethyl group, replaced on isopropyl group in my calculation, then it causes AB easy to form hybridization from staggered conformer to planar  $NH_2BH_2$  by released proton and hydride.

By following the mechanism of proton transfer between ammonia borane and iron complex, I revealed that the steric hindrance of the alkyl groups bonded to phosphorus atoms in

POCOP-pincer ligands strongly effects on the activation barrier. The results are applicable to the other catalytic reactions with similar ligands [59]. The reaction mechanisms of transition metal catalysts are often described in terms of the interaction between the metal center and bonds to fission. As another viewpoint, it is important to understand the influences of the ligands on the reaction path for control the catalytic reactions relevant to hydrogen.



## Chapter 6

### General conclusions

The essence of understanding of mechanism of proton transfer reaction is to find the main point of the whole reaction system by following the reaction path. The explanation for mechanisms of proton transfer is caused with the interpretation of surrounding electronic states because of the relationship with many-body effects.

In order to translate the coordinates obtained by *ab initio* molecular simulations to electronic states information, I used valence bond theory. By the theory, it can be revealed that adjacent  $sp^2$  carbon hybridizations repel the transferred proton.

Not merely in the system constituted by carbon atoms such as graphene, but whatever forms  $sp^2$

hybridization this phenomena seems to occur. In the case of the dehydrogenation reaction in

ammonia borane, the key step of proton transfer in the system is enough space to form planar

$NH_2BH_2$  near the metal center. By following the mechanism of proton transfer between

ammonia borane and iron complex, I made it clear what ligands causes to lower the activation

barrier.

Examine of proton transfer reactions considering the many-body effects make clear the behavior of the number of degrees of freedom around them. It also leads to design the hydrogen transfer reaction paths including catalytic dehydrogenation.



## Acknowledgements

I thank Professor Koichi Yamashita and Associate professor Hiroshi Ushiyama for their advice and suggestion about my work during the doctoral course.

I owe a very important debt to Eriko Watanabe. Dr. Azusa Muraoka has encouraged me in many ways. Dr. Ryota Jono gives me insightful comments and suggestions.

Spetial thanks to Noriki Mizukami, Rinpei Kindaichi, Tomoshi Imamura and Soichiro Ishida as catalyts study group.

I thank Drs. Mikiya Fujii, Yu Xuefang, Kenji Mishima, Giacomo Giorgi, and Katsuhiko Nishimura, Tomoyuki Hata, Ayako Kubo, Seira Hoshino, Ryo Ubagai, Eisuke Kawashima, Chikashi Shinagawa, Masanori Kaneko, Ryo Munakata, Hiroki Iriguchi, Shunsuke Kurahashi, Ryosuke Kodama, Shohei Kouda, Yoshihiro Itou, Tomohiro Yoshihara, Yushiro Kawabe, Noriko Sanpei and Mayumi Iyama for encouragements and daily support in my study life.

I am grateful to the members in Japan Association of Science Communication. Through working with Tatsuya Ogawa, Reiji Takayasu and Tomoyuki Yuzawa, I have considered what I can do for science and scientists.

I also thank Eisuke Tachikawa and his company, NOSIGNER team members, Mayumi

Tokumoto, Takeshi Kawano, Kunihiko Sato, Kaori Hasegawa, Toshiyuki Nakaie and Lyie Nitta. In my internship, they represented the way of working for the benefit of lots of people by my ability as a scientist.

I deeply thank my parents for their daily support.



## Appendix

### Ruthenium and Iron catalysts for dehydrogenation

As one of the catalysts for ammonia borane dehydrogenation reaction, the ruthenium catalyst has been discovered originally developed for alcohol redox processes, and induces the release of 1 equiv. of H<sub>2</sub> [57]. I examined whether rare-metal free iron, homologous with Ru, is reactive with the same ligands.

In order to calculate the energy diagram of the reaction cycle, DFT calculations was performed using the Gaussian 09 program [63]. The structures of all species were optimized using the B3LYP exchange-correlation functional with the mixed basis set, DZVP [60] on Ru and Fe, and TZVP [61] on all other atoms. Tight SCF convergence criteria ( $10^{-8}$  a.u.) were used for all calculations. Harmonic frequency calculations with the analytic evaluation of force constants were used to determine the nature of the stationary points. Free energies of species were evaluated at 298K and 1 atm. Solvent effects were evaluated at the single-point calculations of the solvation energies using the gas-phase geometries. Solvation energies in THF were calculated using the PCM model [62] with the UFF atomic radii. Gibbs free energies in the

solution were estimated by addition of the solvation energy  $\Delta G$  to gas-phase Gibbs free energies.

The energy diagram is shown in Figure A.1. The obtained structures in each steps of iron complexes are almost same as the ruthenium complex structures. The activation energy of the proton transfer reaction is 23.1 kcal mol<sup>-1</sup> on Ru complex, while the barrier height is 23.2 kcal mol<sup>-1</sup> on Fe complex.

The bond lengths of boron-hydrogen attached to the metal centers are elongated of approximately 0.1 Å. NBO analysis reveals that there is charge donation/ back-donation between the metal centers and the boron-hydrogen bonding.

From these results, no major differences can be observed in the energy differences at the rate-determining step and the electronic interactions between the catalysts and ammonia borane, though my calculation cannot refer about the robustness of the catalysts and cycle characteristics.

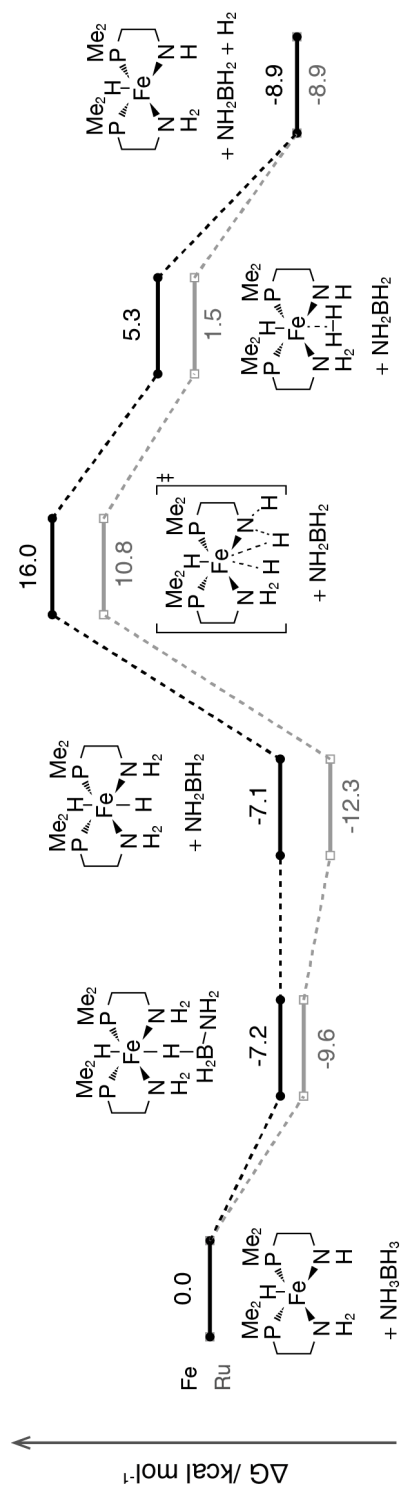


FIGURE A.1: Catalytic cycle for dehydrogenation of AB with the Ru and Fe catalysts in THF from DFT calculations.



## Bibliography

- [1] E. T. J. Nibbering, H. Fidder, and E. Pines, "Ultrafast chemistry: using time-resolved vibrational spectroscopy for interrogation of structural dynamics.," *Annu. Rev. Phys. Chem.*, vol. 56, no. 1, pp. 337–367, 2005.
- [2] M. Eigen, "Proton Transfer, Acid-Base Catalysis, and Enzymatic Hydrolysis. Part I: ELEMENTARY PROCESSES," *Angew. Chemie Int. Ed. English*, vol. 3, no. 1, pp. 1–19, 1964.
- [3] K. Saito, a W. Rutherford, and H. Ishikita, "Mechanism of tyrosine D oxidation in Photosystem II.," *Proc. Natl. Acad. Sci. U. S. A.*, vol. 110, no. 19, pp. 7690–5, 2013.
- [4] S. Hammes-Schiffer and J. C. Tully, "Proton transfer in solution: Molecular dynamics with quantum transitions," *J. Chem. Phys.*, vol. 101, no. 6, p. 4657, Sep. 1994.
- [5] T. Asada, H. Haraguchi, and K. Kitaura, "Simulation Studies of Proton Transfer in N<sub>2</sub> H<sub>7</sub> + Cluster by Classical ab Initio Monte Carlo and Quantum Wave Packet Dynamics," *J. Phys. Chem. A*, vol. 105, no. 31, pp. 7423–7428, Aug. 2001.
- [6] M. E. Tuckerman and D. Marx, "Heavy-Atom Skeleton Quantization and Proton Tunneling in 'Intermediate-Barrier' Hydrogen Bonds," *Phys. Rev. Lett.*, vol. 86, no. 21, pp. 4946–4949, May 2001.
- [7] D. Marx, "Proton transfer 200 years after Von Grotthuss: Insights from ab initio simulations," *ChemPhysChem*, vol. 7, no. 9, pp. 1849–1870, 2006.
- [8] H. Yamataka and M. Aida, "Ab initio direct molecular dynamics simulations and QM/MM computations in search of organic reaction mechanisms," *Bull. Chem. Soc. Jpn.*, vol. 75, no. 12, pp. 2555–2569, 2002.
- [9] G. N. Lewis, "The atom and the molecule," *J. Am. Chem. Soc.*, vol. 38, no. 1913, pp. 762–785, 1916.

- [10] W. Heitler and F. London, "Wechselwirkung neutraler Atome und homöopolare Bindung nach der Quantenmechanik," *Zeitschrift für Phys.*, vol. 44, p. 455–472, 1927.
- [11] R. F. Bader, R. J. Gillespie, and P. J. MacDougall, "A physical basis for the VSEPR model of molecular geometry," *J. Am. Chem. Soc.*, vol. 110, no. 22, pp. 7329–7336, 1988.
- [12] R. S. Mulliken, "Electronic Population Analysis on LCAO[Single Bond]MO Molecular Wave Functions. I," *J. Chem. Phys.*, vol. 23, no. 10, p. 1833, 1955.
- [13] E. A. Reed, R. B. Weinstock, and F. Weinhold, "Natural population analysis," *J. Chem. Phys.*, vol. 83, no. 2, pp. 735–746, 1985.
- [14] A. E. Reed, L. a Curtiss, and F. Weinhold, "Intermolecular interactions from a natural bond orbital, donor-acceptor viewpoint.," *Chem. Rev. (Washington, DC, United States)*, vol. 88, no. 6, pp. 899–926, 1988.
- [15] N. Solcà and O. Dopfer, "Protonated benzene: IR spectrum and structure of  $C_6H_7^+$ ," *Angew. Chemie - Int. Ed.*, vol. 41, no. 19, pp. 3628–3631, 2002.
- [16] D. Schröder, J. Loos, H. Schwarz, R. Thissen, and O. Dutuit, "Protonated benzene: A case for structural memory effects?," *J. Phys. Chem. A*, vol. 108, no. 45, pp. 9931–9937, 2004.
- [17] M. Head-Gordon, J. A. Pople, and M. J. Frisch, "MP2 energy evaluation by direct methods," *Chem. Phys. Lett.*, vol. 153, no. 6, pp. 503–506, Dec. 1988.
- [18] S. Sæbø and J. Almlöf, "Avoiding the integral storage bottleneck in LCAO calculations of electron correlation," *Chem. Phys. Lett.*, vol. 154, no. 1, pp. 83–89, Jan. 1989.
- [19] M. J. Frisch, M. Head-Gordon, and J. A. Pople, "A direct MP2 gradient method," *Chem. Phys. Lett.*, vol. 166, no. 3, pp. 275–280, Feb. 1990.
- [20] M. J. Frisch, M. Head-Gordon, and J. A. Pople, "Semi-direct algorithms for the MP2 energy and gradient," *Chem. Phys. Lett.*, vol. 166, no. 3, pp. 281–289, Feb. 1990.

- [21] M. Head-Gordon and T. Head-Gordon, "Analytic MP2 frequencies without fifth-order storage. Theory and application to bifurcated hydrogen bonds in the water hexamer," *Chem. Phys. Lett.*, vol. 220, no. 1–2, pp. 122–128, Mar. 1994.
- [22] C. Møller and M. S. Plesset, "Note on an approximation treatment for many-electron systems," *Phys. Rev.*, vol. 46, no. 7, pp. 618–622, 1934.
- [23] P. Hohenberg, "Inhomogeneous Electron Gas," *Phys. Rev.*, vol. 136, no. 3B, pp. B864–B871, Nov. 1964.
- [24] W. Kohn and L. J. Sham, "Self-Consistent Equations Including Exchange and Correlation Effects," *Phys. Rev.*, vol. 140, no. 4A, pp. A1133–A1138, Nov. 1965.
- [25] R. G. Parr and W. Yang, *Density-Functional Theory of Atoms and Molecules*. Oxford: Oxford Univ. Press, 1989.
- [26] C. Lee, W. Yang, and R. G. Parr, "Development of the Colle-Salvetti correlation-energy formula into a functional of the electron density," *Phys. Rev. B*, vol. 37, no. 2, pp. 785–789, Jan. 1988.
- [27] A. D. Becke, "Density-functional thermochemistry. III. The role of exact exchange," *J. Chem. Phys.*, vol. 98, no. 7, p. 5648, Apr. 1993.
- [28] G. a Olah, R. H. Schlosberg, R. D. Porter, Y. K. Mo, D. P. Kelly, and G. D. Mateescu, "Stable Carbocations CXXIV The Benzenium Ion and Monoalkylbenzenium Ions," *J. Am. Chem. Soc.*, vol. 94, no. 6, pp. 2034–2043, 1972.
- [29] D. Marx and J. Hutter, *Ab initio molecular dynamics: Theory and implementation*, vol. 1. 2000.
- [30] M. W. Schmidt, "General atomic and molecular electronic structure system," *J. Comput. Chem.*, vol. 14, no. 11, pp. 1347–1363, 1993.
- [31] J. C. Butcher, *Numerical Methods for Ordinary Differential Equations*. New York, 2003.
- [32] J. I. Steinfeld, J. S. Francisco, and W. L. Hase, *Chemical Kinetics and Dynamics*. Prentice Hall, 1998.

- [33] O. K. Rice and H. C. Ramsperger, "THEORIES OF UNIMOLECULAR GAS REACTIONS AT LOW PRESSURES. II," *J. Am. Chem. Soc.*, vol. 50, no. 3, pp. 617–620, Mar. 1928.
- [34] L. S. Kassel, "Studies in Homogeneous Gas Reactions. II. Introduction of Quantum Theory," *J. Phys. Chem.*, vol. 32, no. 7, pp. 1065–1079, Jan. 1927.
- [35] M. Berblinger and C. Schlier, "How accurate is the Rice–Ramsperger–Kassel–Marcus theory? The case of  $H_3^+$ ," *J. Chem. Phys.*, vol. 101, no. June, pp. 4750–4758, 1994.
- [36] S. G. Shore and R. W. Parry, "The Crystalline Compound Ammonia-Borane,  $NH_3BH_3$ ," *J. Am. Chem. Soc.*, vol. 77, no. 4, pp. 6084–6085, 1955.
- [37] M. C. Denney, V. Pons, T. J. Hebden, D. M. Heinekey, and K. I. Goldberg, "Efficient catalysis of ammonia borane dehydrogenation," *J. Am. Chem. Soc.*, vol. 128, no. 37, pp. 12048–12049, 2006.
- [38] R. T. Baker, J. C. Gordon, C. W. Hamilton, N. J. Henson, P. H. Lin, S. Maguire, M. Murugesu, B. L. Scott, and N. C. Smythe, "Iron complex-catalyzed ammonia-borane dehydrogenation. A potential route toward B-N-containing polymer motifs using earth-abundant metal catalysts," *J. Am. Chem. Soc.*, vol. 134, no. 12, pp. 5598–5609, 2012.
- [39] S. K. Kim, W. S. Han, T. J. Kim, T. Y. Kim, S. W. Nam, M. Mitoraj, L. Piekoś, A. Michalak, S. J. Hwang, and S. O. Kang, "Palladium catalysts for dehydrogenation of ammonia borane with preferential b-h activation," *J. Am. Chem. Soc.*, vol. 132, no. 29, pp. 9954–9955, 2010.
- [40] B. L. Conley, D. Guess, and T. J. Williams, "A robust, air-stable, reusable ruthenium catalyst for dehydrogenation of ammonia borane," *J. Am. Chem. Soc.*, vol. 133, no. 36, pp. 14212–14215, 2011.
- [41] X. Hu, M. Soleilhavoup, M. Melaimi, J. Chu, and G. Bertrand, "Air-Stable (CAAC)CuCl and (CAAC)CuBH<sub>4</sub> Complexes as Catalysts for the Hydrolytic Dehydrogenation of  $BH_3NH_3$ ," *Angew. Chemie*, p. n/a–n/a, 2015.

- [42] P. M. Zimmerman, A. Paul, Z. Zhang, and C. B. Musgrave, "The Role of Free N-Heterocyclic Carbene ( NHC ) in the Catalytic Dehydrogenation of Ammonia – Borane in the Nickel NHC System," pp. 2201–2205, 2009.
- [43] A. D. Sutton, A. K. Burrell, D. A. Dixon, E. B. G. III, J. C. Gordon, T. Nakagawa, K. C. Ott, J. P. Robinson, and M. Vasiliu, "Regeneration of Ammonia Borane Spent Fuel by Direct Reaction with Hydrazine and Liquid Ammonia," *Science*, vol. 331, no. 2011, pp. 1426–1429, 2011.
- [44] P. Bhattacharya, J. A. Krause, and H. Guan, "Mechanistic studies of ammonia borane dehydrogenation catalyzed by iron pincer complexes," *J. Am. Chem. Soc.*, vol. 136, no. 31, pp. 11153–11161, 2014.
- [45] Y. Zhao and D. G. Truhlar, "Improved Description of Nuclear Magnetic Resonance Chemical Shielding Constants Using the M06-L Meta-Generalized-Gradient-Approximation Density Functional," *Society*, vol. 112, no. 30, pp. 6794–6799, 2008.
- [46] D. Jacquemin, E. a. Perpète, I. Ciofini, C. Adamo, R. Valero, Y. Zhao, and D. G. Truhlar, "On the performances of the M06 family of density functionals for electronic excitation energies," *J. Chem. Theory Comput.*, vol. 6, no. 7, pp. 2071–2085, 2010.
- [47] C. S. Lo, "Performance of density functional theory on homogeneous gold catalysis," pp. 647–661, 2011.
- [48] P. J. Hay and W. R. Wadt, "Ab initio effective core potentials for molecular calculations. Potentials for K to Au including the outermost core orbitals," *J. Chem. Phys.*, vol. 82, no. 1, pp. 299–310, 1985.
- [49] W. R. Wadt and P. J. Hay, "Ab initio effective core potentials for molecular calculations. Potentials for main group elements Na to Bi," *J. Chem. Phys.*, vol. 82, no. 1, pp. 284–298, 1985.
- [50] A. W. Ehlers, M. Böhme, S. Dapprich, A. Gobbi, A. Höllwarth, V. Jonas, K. F. Köhler, R. Stegmann, A. Veldkamp, and G. Frenking, "A set of f-polarization functions for pseudo-potential basis sets of the transition metals Sc-Cu, Y-Ag and La-Au," *Chem. Phys. Lett.*, vol. 208, no. 1–2, pp. 111–114, 1993.

- [51] A. Höllwarth, M. Böhme, S. Dapprich, A. W. Ehlers, A. Gobbi, V. Jonas, K. F. Köhler, R. Stegmann, A. Veldkamp, and G. Frenking, "A set of d-polarization functions for pseudo-potential basis sets of the main group elements Al-Bi and f-type polarization functions for Zn, Cd, Hg," *Chem. Phys. Lett.*, vol. 208, no. 3–4, pp. 237–240, 1993.
- [52] R. S. Mulliken, "A New Electroaffinity Scale: Together with Data on Valence States And Ionization Potential and Electron Affinities," *J. Chem. Phys.*, vol. 2, pp. 782–793, 1934.
- [53] M. Cossi, V. Barone, B. Mennucci, and J. Tomasi, "Ab initio study of ionic solutions by a polarizable continuum dielectric model," *Chem. Phys. Lett.*, vol. 286, no. 3–4, pp. 253–260, 1998.
- [54] E. Cancès, B. Mennucci, and J. Tomasi, "A new integral equation formalism for the polarizable continuum model: Theoretical background and applications to isotropic and anisotropic dielectrics," *J. Chem. Phys.*, vol. 107, no. 8, p. 3032, 1997.
- [55] B. Mennucci and J. Tomasi, "Continuum solvation models: A new approach to the problem of solute s charge distribution and cavity boundaries," *J. Chem. Phys.*, vol. 106, no. 12, pp. 5151–5158, 1997.
- [56] L. C. Li, J. X. Jiang, J. Ren, Y. Ren, C. U. Pittman, and H. J. Zhu, "Unexpected selectivity in sodium borohydride reductions of  $\alpha$ -substituted esters: Experimental and theoretical studies," *European J. Org. Chem.*, no. 8, pp. 1981–1990, 2006.
- [57] N. Blaquiere, S. Diallo-Garcia, S. I. Gorelsky, D. A. Black, and K. Fagnou, "Ruthenium-catalyzed dehydrogenation of ammonia boranes," *J. Am. Chem. Soc.*, vol. 130, no. 43, pp. 14034–14035, 2008.
- [58] V. M. Bzhezovskii, E. G. Kapustin, and L. M. Yagupol, "Steric and Electronic Structure of  $C_6H_5XCF_3$  Molecules ( X = O or S ): A Quantum-Chemical Study," *Russ. J. Gen. Chem.*, vol. 73, no. 2, pp. 229–239, 2003.
- [59] M. Montag, I. Efremenko, R. Cohen, L. J. W. Shimon, G. Leitun, Y. Diskin-Posner, Y. Ben-David, H. Salem, J. M. L. Martin, and D. Milstein, "Effect of CO on the oxidative addition of arene C-H bonds by cationic rhodium complexes," *Chem. - A Eur. J.*, vol. 16, no. 1, pp. 328–353, 2010.

- [60] N. Godbout, D. R. Salahub, J. Andzelm, and E. Wimmer, "Optimization of Gaussian-type basis sets for local spin density functional calculations. Part I. Boron through neon, optimization technique and validation," *Can. J. Chem.*, vol. 70, no. 2, pp. 560–571, 1992.
- [61] A. Schäfer, C. Huber, and R. Ahlrichs, "Fully optimized contracted Gaussian basis sets of triple zeta valence quality for atoms Li to Kr," *J. Chem. Phys.*, vol. 100, no. 8, pp. 5829–5835, 1994.
- [62] V. Barone, M. Cossi, and J. Tomasi, "Geometry optimization of molecular structures in solution by the polarizable continuum model," *J. Comput. Chem.*, vol. 19, no. 4, pp. 404–417, 1998.
- [63] Gaussian 09, Revision D.01, M. J. Frisch, G. W. Trucks, H. B. Schlegel, G. E. Scuseria, M. A. Robb, J. R. Cheeseman, G. Scalmani, V. Barone, B. Mennucci, G. A. Petersson, H. Nakatsuji, M. Caricato, X. Li, H. P. Hratchian, A. F. Izmaylov, J. Bloino, G. Zheng, J. L. Sonnenberg, M. Hada, M. Ehara, K. Toyota, R. Fukuda, J. Hasegawa, M. Ishida, T. Nakajima, Y. Honda, O. Kitao, H. Nakai, T. Vreven, J. A. Montgomery, Jr., J. E. Peralta, F. Ogliaro, M. Bearpark, J. J. Heyd, E. Brothers, K. N. Kudin, V. N. Staroverov, R. Kobayashi, J. Normand, K. Raghavachari, A. Rendell, J. C. Burant, S. S. Iyengar, J. Tomasi, M. Cossi, N. Rega, J. M. Millam, M. Klene, J. E. Knox, J. B. Cross, V. Bakken, C. Adamo, J. Jaramillo, R. Gomperts, R. E. Stratmann, O. Yazyev, A. J. Austin, R. Cammi, C. Pomelli, J. W. Ochterski, R. L. Martin, K. Morokuma, V. G. Zakrzewski, G. A. Voth, P. Salvador, J. J. Dannenberg, S. Dapprich, A. D. Daniels, Ö. Farkas, J. B. Foresman, J. V. Ortiz, J. Cioslowski, and D. J. Fox, Gaussian, Inc., Wallingford CT, 2009.